Journal of Physics D: Applied Physics

Synthesis and Recent Developments of MXene-Based Composites for Photocatalytic Hydrogen Production

To cite this article before publication: Yifan Liao *et al* 2024 *J. Phys. D: Appl. Phys.* in press https://doi.org/10.1088/1361-6463/ad7470

Synthesis and Recent Developments of MXene-Based Composites for Photocatalytic Hydrogen Production

Yifan Liao, Xinglin Wang, Huajun Gu, Huihui Zhang, Jiayi Meng, Wei-Lin Dai*

Department of Chemistry and Shanghai Key Laboratory of Molecular Catalysis and Innovative Materials, Fudan University, Shanghai 200433, P. R. China

***Corresponding author: Prof. & Dr. Wei-Lin Dai**

Fax: +86 3124 2978

Tel: +86 3124 9122

E-mail: wldai@fudan.edu.cn

Abstract

The energy crisis has already seriously affected the daily lives of people around the world. As a result, designing efficient catalysts for photocatalytic hydrogen evolution is a promising strategy to energy supply. Co-catalyst modification can significantly enhance the photocatalytic activity of single semiconductors, overcoming limitations posed by their narrow visible light absorption range and high electron-hole recombination rate. MXene-based composites demonstrate immense potential as co-catalysts for photocatalytic hydrogen production owing to their distinctive two-dimensional layered structure and outstanding photoelectrochemical properties, and further research and development efforts surrounding MXene-based composites will contribute significantly to the progress of sustainable energy technologies. In this review, we offers a comprehensive overview of synthesis methods for MXene and MXene-based composites, highlights illustrative instances of binary and ternary MXene-based composites in photocatalytic hydrogen evolution, and explores potential avenues for future research and expansion of MXene-based composites.

Keywords: Photocatalysis; MXene; MXene-based composites; Synthesis methods; Co-catalyst; Photocatalytic hydrogen evolution.

1. Introduction

Given that fossil fuels continue to be the primary energy source in nearly all countries' energy portfolios, their extended formation cycle and the emission of harmful gases during combustion pose significant obstacles to their utilization in sustainable development efforts. As an ideal form of energy, hydrogen is promising in the energy revolution on account of its high calorific value, beneficial product–H_2O, and extensive sources. At the current stage, the primary hydrogen production technologies include methane steam reforming, coal gasification, methanol steam reforming, water electrolysis, and photocatalytic water splitting. The first three of these technologies can be collectively classified as thermochemical hydrogen production methods and methane reforming is currently the most mature hydrogen production technology. However, these methods are often accompanied by the emission of carbon-containing compounds such as CO and CO_2, which is unfavorable for sustainable development and environmental protection. On the other hand, the process of water electrolysis for hydrogen production requires a significant amount of electrical energy, and the construction of the electrolysis system necessitates the use of high-purity materials, resulting in higher costs. Additionally, methods like steam methane reforming and electrolysis rely on external heat or electrical energy inputs, leading to additional energy losses. In contrast, photocatalysis directly utilizes solar energy, a clean form of energy, and converts it into chemical energy so that it has the potential to achieve high conversion rates and energy efficiencies [1]. However, due to the inadequacies in the design of catalysts and the exploration of reaction conditions, the efficiency of photocatalytic water splitting for hydrogen production remains suboptimal. Technical

challenges, such as the large-scale deposition of photocatalysts and the expansion of photoreactor dimensions, are currently posing key obstacles to the scaled-up production and application of photocatalytic technology. Therefore, the development of efficient, stable, and cost-effective photocatalysts remains a significant challenge in optimizing the efficiency of photocatalytic water splitting for hydrogen production.

To date, various photocatalysts are under extensive research, such as transition metal oxides [4], g-C_3N_4 [7], transition metal sulfides [10], Bi-based photocatalysts [13], covalent-organic frameworks (COFs) [16] and metal-organic frameworks (MOFs) [19]. Nevertheless, the catalytic efficiency of single-component photocatalysts is constrained by their limited sunlight utilization and high electron-hole recombination rates. Therefore, researchers attempt to enhance the photocatalytic performance through modification strategies. Co-catalyst modification serves as a primary means to expedite surface redox kinetics and optimize charge transfer. The photocatalytic water splitting process involving the co-catalyst is depicted in Scheme 1. Under visible light irradiation, when the photon energy is equivalent to or exceeds the band gap of the semiconductor photocatalyst, the photon is absorbed. This causes the electrons in the valence band (VB) to be stimulated and transferred to the conduction band (CB), leaving behind holes in the VB. The close contact between the co-catalyst and the semiconductor enables it to act as an electron trap, facilitating the rapid transfer of photogenerated electrons to the co-catalyst, which promotes the separation of electrons and holes and reduces the recombination of photogenerated carriers. In this case, the co-catalyst provides reactive sites for reduction reaction, converting H^+ to H_2, while the holes in the VB of

the semiconductor participate in the oxidation reaction to produce oxygen or are consumed by the sacrificial agent to complete the whole photocatalytic hydrogen production reaction. Notably, noble metals, including Pt and Au, are commonly employed as reduction co-catalysts, whereas oxides or hydroxides of Co and Mn exhibit exceptional performance as oxidation co-catalysts [22]. Despite their potential, the significant cost, intricate processing, and inconsistent photocatalytic performance of these cocatalysts render them unsuitable for practical applications. Therefore, it is imperative to explore efficient and cost-effective alternatives to these co-catalysts. MXene, initially synthesized and presented by Gogotsi in 2011 [26], pertains to a class of two-dimensional (2D) materials encompassing transition metal carbides, nitrides, and carbon-nitrides, that possess exceptional metallic conductivity and appropriate Fermi energy levels. They usually contain -F, -O, and -OH functional groups on the surface [27], which is favorable for combining with semiconductor photocatalysts to serve as a co-catalyst. These properties and expanded specific surface area can significantly reduce the carrier transport distance, expedite carrier migration, and ultimately enhance the photocatalytic hydrogen production activity of the catalysts [28]. Therefore, it is essential to provide a comprehensive overview that focuses on recently reported MXene-based composites for the photocatalytic hydrogen evolution reaction (PHE).

In this review, we offer an exposition on the synthesis methods and latest advancements pertaining to MXene-based composites, emphasizing their applications as co-catalysts in PHE. Firstly, we summarize several common synthetic methods for MXenes and the subsequent preparation of MXene-based photocatalysts. Then, we analyze and review how different types

of MXene-based composites work in PHE based on recent research works. Finally, conclusions and an outlook on the challenges, prospects and potential applications for MXene-based composites in developing sustainable hydrogen energy are discussed.

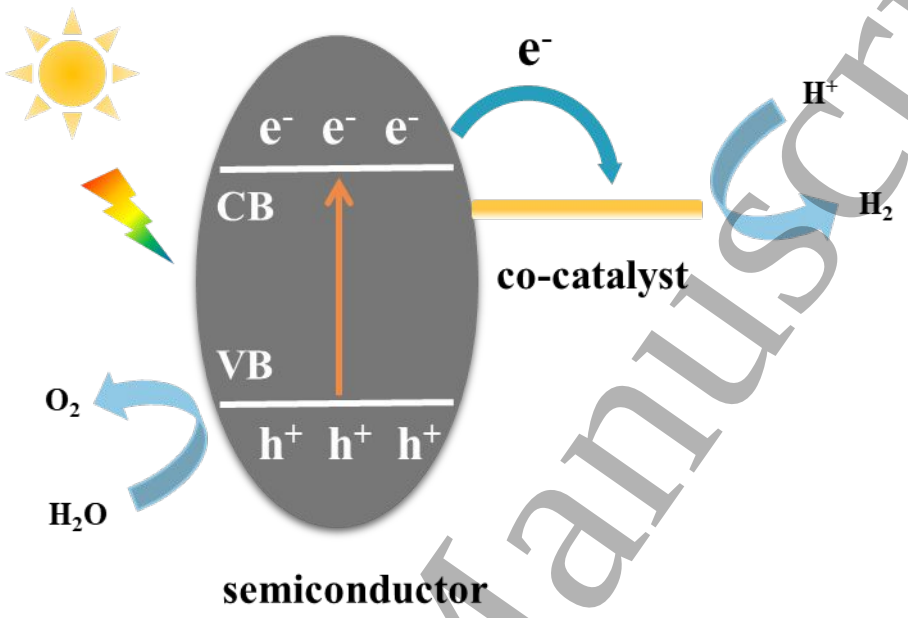

Scheme 1. Schematic illustration of the photocatalytic H_2 production mechanism of semiconductors composite with co-catalysts.

2. Synthesis methods of MXenes and MXene-based composites

The traditional method for synthesizing MXene is HF etching. In response to increasing demands for sustainability and environmental protection, researchers have proposed milder and greener synthesis methods, such as using LiF/HCl mixed solutions instead of HF, thermal reduction, and chemical vapor deposition. MXene-based composites are typically formed by first synthesizing MXene and then combining it with other materials, primarily through methods such as physical mixing, electrostatic self-assembly, in-situ hydrothermal/ solvothermal synthesis and so on.

2.1 Synthesis of MXenes

MXene was initially reported as being procured through the removal of **A** element from the precursor MAX phase by HF etching, in which **M** stands for an early transition metal element (such as Ti, Zr, Sc, V, Nb and Mo), **A** represents an element from group 13 or 14 (such as Al, Ga, In, Sn, etc.), while **X** denotes a carbon or nitrogen atom [26]. As shown in Figure 1a, since the M-A bond is less robust than M-X, HF is able to selectively destroy M-A, and the end result is that the **A** atomic layer is stripped off to generate multilayer MXenes. Multilayer MXenes can be separated by sonication of the solution, on the basis of which fewer-layered or even single-layered MXenes can be obtained through manual shaking or mechanical stirring [29]. In view of the extreme corrosiveness of HF, a safer and more efficient etching method that replaces the conventional HF etching method with a LiF/HCl system is more widely used [30]. Furthermore, hydrothermal etching with aqueous NaOH can avoid the use of F-containing reagents and obtain MXenes without -F terminals [31]. As the study progressed, researchers found that the use of intercalators such as isopropylamine (IPA) [32], dimethyl sulfoxide (DMSO) [33], tetrabutylammonium hydroxide (TBAOH) [34], tetramethylammonium hydroxide (TMAOH) [35] and so on, could be embedded between MXene layers to disrupt the weak interactions, thereby facilitating the peeling of single-layered MXenes.

In addition to the conventional etching method using HF as the main etchant, MXene can also be synthesized by other routes to avoid the generation of etch-related hazardous waste. One of the facile and efficient methods is thermal reduction. Ti_2C was synthesized from sulphur-containing Ti_2SC MAX phase at the optimum reduction temperature of 800 °C by Mei

et al. [36]. In this process, S species were selectively removed from the Ti_2SC MAX phase by thermal reduction under a H_2 atmosphere and then the intermediate was ultrasound-assisted delaminated into monolayer MXene, as shown in Figure 1b. The extraction of relatively inert sulphur from the corresponding sulphur-containing MAX frameworks by thermal reduction offers a novel method for fabricating 2D MXene and makes large-scale production possible. Recently, Wang et al. described a synthetic approach for vertically growing MXene on metal foil's surface, employing the chemical vapor deposition (CVD) method [37]. Ti_2CCl_2 was obtained by a gaseous blend of CH_4 and $TiCl_4$ diluted in Ar reacting at 950 °C on Ti foil and Ti_2NCl_2, Zr_2CCl_2 and Zr_2CBr_2 MXenes are also successfully prepared through a similar process. This method allows the direct synthesis of MXene in the absence of the MAX phase, which greatly saves time and provides new opportunities to obtain novel MXenes that cannot be synthesized through conventional etching methods.

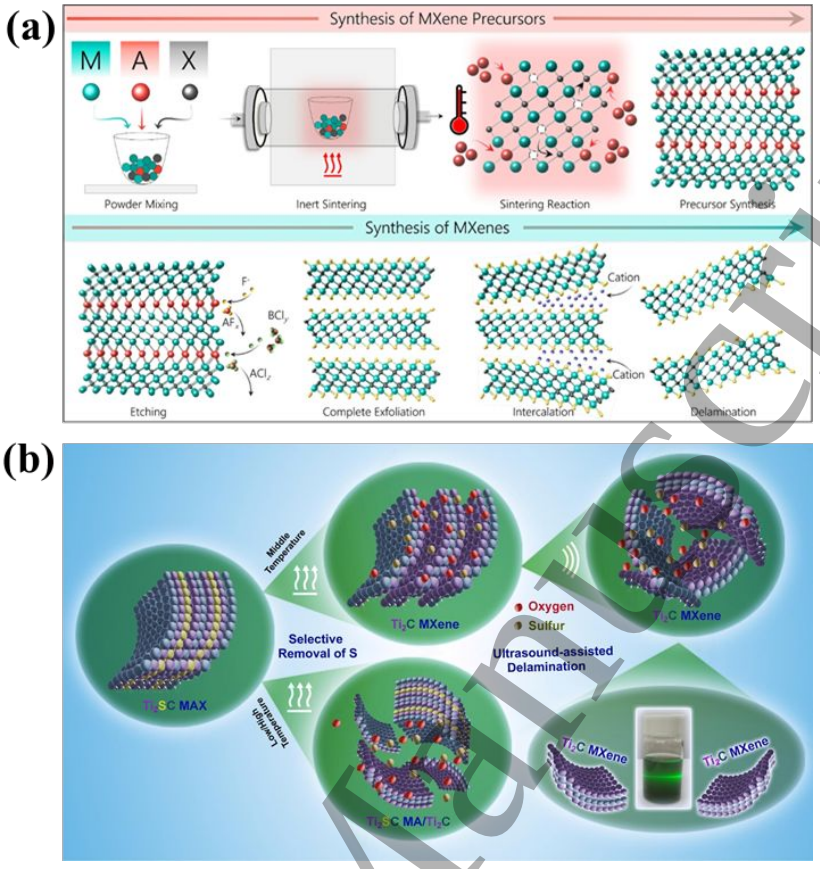

Figure 1. (a) Synthesis of MAX phase and MXene [29]. Copyright 2022 Springer Nature. (b) Schematic illustration of the fabrication of 2D Ti_2C MXene [36]. Copyright 2020 Elsevier.

2.2 Synthesis of MXene-based composites

MXene has limited photocatalytic activity and is primarily used as a co-catalyst in combination with other common photocatalysts in photocatalysis. Summarizing the existing methods of composite preparation can provide a reference for subsequent research. Due to the special conditions for the synthesis of MXene, MXene-based composites are usually synthesised first and then composited with semiconductor materials by other methods. A wide variety of MXene composites have emerged, but in general, there are three main methods of synthesis.

2.2.1 Physical mixing

Physical mixing, which mainly refers to combining two pre-prepared components by mechanical grinding or stirring in the liquid phase, is one of the simplest methods to form composite photocatalysts. This method boasts advantages such as brevity in reaction time, ease of implementation, and cost-effectiveness. However, MXenes have a tendency to agglomerate due to their high surface energy, which can lead to non-uniform composites with inconsistent properties. At the same time, physical mixing often results in weak interfacial interactions between MXenes and the other material. According to Sherryna et al. [38], g-C_3N_4 powder and prepared V_2C were dispersed and parallel stirred in methanol and then dried overnight to acquire V_2C/g-C_3N_4 2D/2D nanohybrids, as demonstrated in Figure 2. As for the morphology of the composite, the g-C_3N_4 sheets were inserted between the vanadium-containing layers of the V_2C, and the 2D structure of V_2C provides a favourable platform for g-C_3N_4 attachment as well as reduces the aggregation of g-C_3N_4 nanosheets so that it can successfully grow on the V_2C interval layer. Due to the remarkable conductivity of V_2C, an interfacial potential energy barrier is formed at the Schottky junction of the composite, in which V_2C functions as an electron trapper, efficiently suppressing the recombination of carriers.

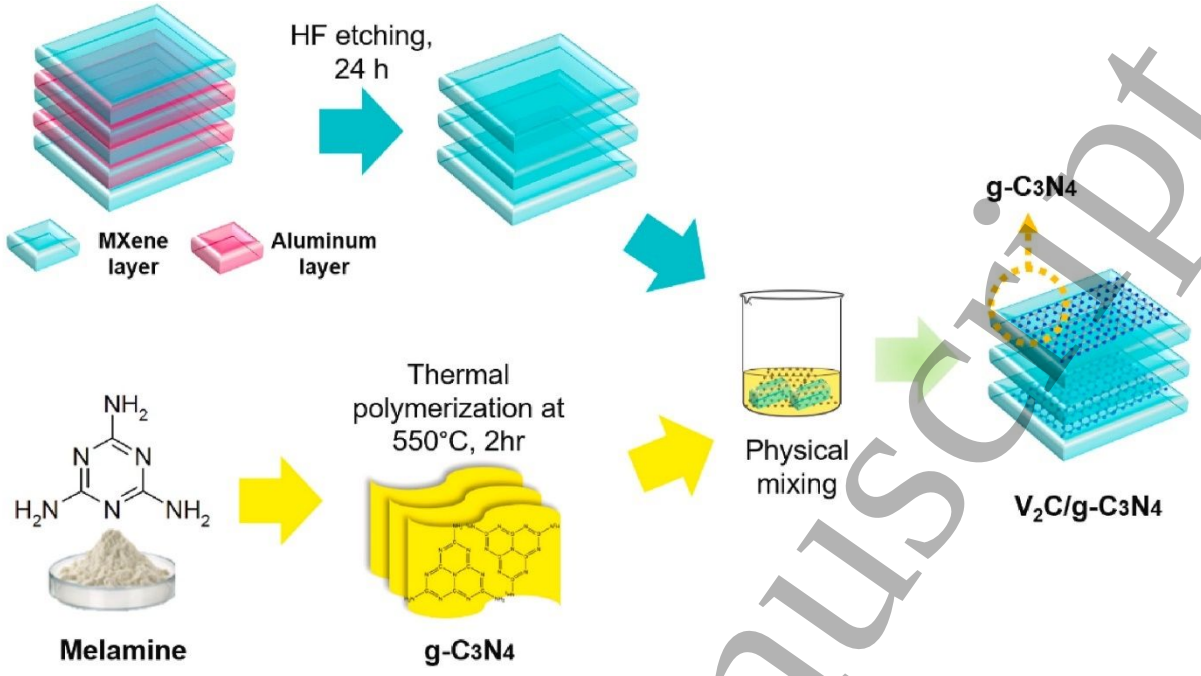

Figure 2. Schematic illustration for the synthesis of V_2C/g-C_3N_4 [38]. Copyright 2024 Elsevier.

2.2.2 Electrostatic self-assembly

Electrostatic self-assembly is a phenomenon of substance aggregation that occurs spontaneously on account of the mutual attraction between opposing charges. Compared with physical mixing, the components of the complex obtained by this method are in closer contact with each other and more evenly dispersed [39]. The process can be sensitive to environmental factors such as pH, ionic strength, and temperature, which can affect the reproducibility and uniformity of the composites.

Li et al. [40] prepared Ti_3C_2 quantum dots through etching Ti_3AlC_2 MAX phase with hydrofluoric acid solution followed by sonication in DMSO, addition of polyethyleneimine (PEI) and finally hydrothermal preparation under N_2 atmosphere. The pre-prepared porous graphitic carbon nitride (PGCN) was subsequently dispersed in aqueous solution and Ti_3C_2

quantum dots were then added to prepare Ti_3C_2 QD/PGCN with electrostatic self-assembly, as illustrated in Figure 3. The Ti_3C_2 quantum dots in the Ti_3C_2 QD/PGCN samples synthesized by the above route are evenly attached to PGCN, while the inherent 3D macroporous structure of the PGCN remains intact. Given the strong localized surface plasmon resonance (LSPR) phenomenon, Ti_3C_2 QDs are able to enhance the optical absorption range and carrier density of the composite. Furthermore, the work function of Ti_3C_2 quantum dot exceeds that of PGCN, resulting in spontaneous electron transfer from PGCN to Ti_3C_2 quantum dots, thereby significantly improving the segregation of photogenerated carriers. Additionally, the 3D porous architecture of PGCN offers a superior permeation rate and extensive specific surface area, enabling efficient carrier migration at a rapid pace. The ultimate outcome demonstrates that 5.5 wt% Ti_3C_2 QD/PGCN achieves a remarkable hydrogen production rate of 4040.95 μmol g^{-1} h^{-1}, surpassing the rate of PGCN by a factor of over 3.53. Ruan et al. [41] constructed a-TiO_2/H-TiO_2/Ti_3C_2 (MXTi) ternary heterojunction composite by electrostatic self-assembly method. A type II homojunction is established between H-TiO_2 and a-TiO_2. During the photocatalytic hydrogen production reaction, photogenerated electrons transfer from H-TiO_2 to a-TiO_2 and finally to Ti_3C_2. Conversely, holes transfer from a-TiO_2 to H-TiO_2. MXene serves as an electron acceptor, driving the reduction of protons to hydrogen. This study reveals that the combination of interfacial engineering and MXene as a co-catalyst exhibits a synergistic effect, resulting in a notable increase in the photocatalytic hydrogen production activity of the composite.

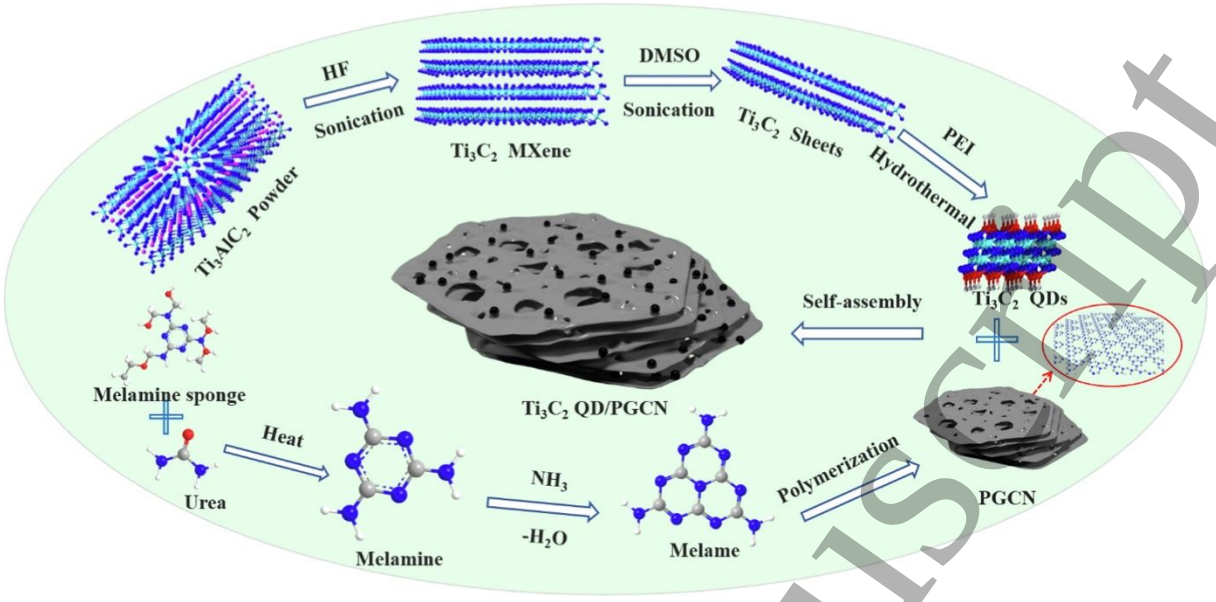

Figure 3. Schematic illustration for preparing Ti_3C_2 QD/PGCN composites [40]. Copyright 2023 Elsevier.

2.2.3 In-situ hydrothermal/ solvothermal synthesis

Currently, the in situ hydrothermal method stands as the preferred technique for synthesizing MXene-based complexes [42], and components prepared by this approach are chemically bonded to each other, thus allowing the synthesis of composites with high crystallinity and predictable shapes. However, MXene is susceptible to oxidation in solution, particularly at elevated temperatures. Consequently, the preparation process often necessitates the use of gentler conditions. At the same time, the need for specialized high-pressure reactors limits the scalability of this method. Large-scale production requires reactors that can uniformly maintain high pressure and temperature, which is both challenging and costly.

Sun et al. [43] successfully synthesized 1D/2D CdS nanorod@Ti_3C_2 MXene (CdS@Ti_3C_2) through an in-situ hydrothermal process with CdS nanorod (NRs) uniformly distributed on the

surface of Ti_3C_2 MXene nanosheets (NSs), as shown in Figure 4. Regarding the CdS@Ti_3C_2 composites, CdS exhibits an advantageous energy band structure and remarkable electron-reducing capabilities, while Ti_3C_2-MXene NSs possess strong electron-transferring properties and accordion-like multilayers, thus offering a greater number of reactive sites. The close interfacial contact established between CdS nanorods and Ti_3C_2 MXene efficiently reduce the carrier migration distance, leading to an acceleration in the movement of photogenerated carriers. It is noteworthy that the catalysts mentioned above possess good photocatalytic nitrogen fixation activity in addition to high photocatalytic hydrogen production activity. Zuo et al. [44] synthesized sandwich-like hierarchical heterostructures ultrathin $ZnIn_2S_4$ nanosheets-MXene ($Ti_3C_2T_x$) nanosheets-ultrathin $ZnIn_2S_4$ nanosheets (UZNs-MNs-UZNs) in a glycerol aqueous solution at 80 °C. During this procedure, MXene ($Ti_3C_2T_x$) nanosheets (MNs) functioned as a substrate for the in-situ growth of ultrathin $ZnIn_2S_4$ nanosheets (UZNs) and the UZNs could be uniformly epitaxialized and grown on both surfaces of the MNs. The hierarchical heterostructure of UZNs-MNs-UZNs (MNZIS) has a larger specific surface area and pore size compared to pristine $ZnIn_2S_4$, exhibits enhanced hydrophilicity and is able to provide richer reaction sites for photocatalytic hydrogen production reactions, which is beneficial to the photocatalytic activity. Zhang et al. [45] successfully constructed $SrTiO_3$/Ti_3C_2 MXene (STO/TC) Schottky heterojunctions through etching Ti atoms from the surface of Ti_3C_2 MXene (TC) with $Sr(OH)_2$, followed by the in situ growth of $SrTiO_3$ (STO) on Ti_3C_2 MXene under hydrothermal conditions. The above reaction resulted in the uniform anchoring of $SrTiO_3$ nanoparticles onto 2D Ti_3C_2 MXene nanosheets, forming a tightly

chemically bonded interface between them. During the in-situ growth process of $SrTiO_3$, certain Ti-C bonds within Ti_3C_2 MXene were cleaved, resulting in the creation of Ti vacancies. These vacancies serve as efficient catalytically active sites, facilitating the transfer of charge carriers and enhancing the photocatalytic hydrogen production process.

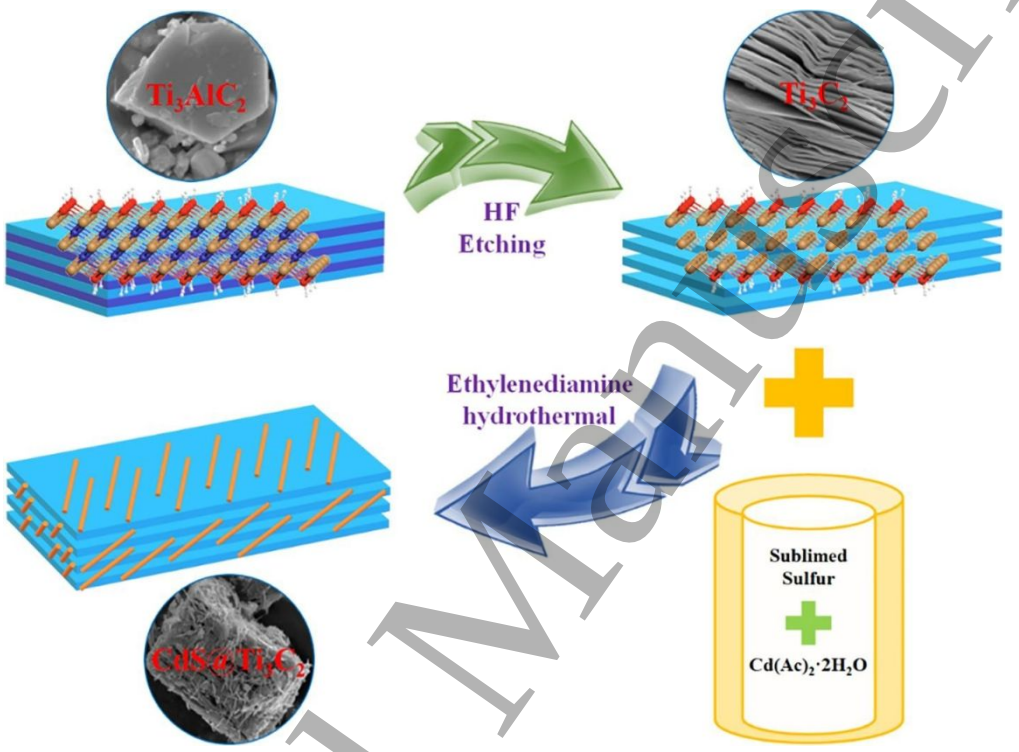

Figure 4. Schematic illustration of the fabrication of $CdS@Ti_3C_2$ composites [43]. Copyright 2021 Elsevier.

Apart from the aforementioned synthetic approaches for MXene-based composites, calcination under N_2 atmosphere [46], high-energy ball milling [48] and wet chemical oxidation are also available [49]. It is crucial to acknowledge that MXene is prone to oxidation. Consequently, during the preparation of MXene-based composites, utmost care must be exercised in selecting appropriate conditions to prevent its oxidation and thereby maintain its chemical stability.

3. Applications of MXene-based composites for photocatalytic hydrogen evolution

MXene, as an emerging functional material, has been widely used in catalysis [50], sensors [53], energy storage [56], biomedical science [59] and other fields. Owing to its large specific surface area, superior electrical conductivity, and abundance of surface functional groups, MXene-based composites emerge as an ideal co-catalyst for photocatalysis. It plays a crucial role in various fields, including photocatalytic hydrogen evolution [38], CO_2 reduction [62], nitrogen fixation [63] and pollutant degradation [64]. Here, we highlight and summarize the latest advancements in the utilization of MXene-based composites for photocatalytic hydrogen evolution.

3.1 Binary composites

MXene serves as a co-catalyst, responsible for accepting electrons and functioning in the photocatalytic hydrogen production reaction primarily by complexing with semiconductor materials, such as transition metal oxides (TMO), transition metal sulfides and selenides (TMSS), g-C_3N_4, organics, etc.

3.1.1 Composite with TMO

Since TiO_2 was first discovered to absorb ultraviolet light and catalyze the decomposition of water to produce hydrogen in 1972 [65], transition metal oxides have set off a boom in the field of photocatalysis. However, their photocatalytic activity is constrained by the large band gaps, narrow absorption range of light, and the swift recombination rate of electrons and holes. In order to address these constraints, a series of new advances have been made in recent years

on the participation of MXene complexed with TMOs in photocatalytic hydrogen production. TiO_2, as the first discovered photocatalytically active metal oxide, has also been most widely studied for its composite modification with Ti_3C_2 MXene [66]. However, there have been few studies on the influence of MXene's surface groups on the performance of co-catalysts in photocatalytic reactions. The surface terminations of MXene determine its work function and Gibbs free energy of the hydrogen radical [69], and therefore, MXenes with different surface termination play different roles in the photocatalysis of composites. Wang et al. [70] prepared urchin-like $TiO_2/Ti_3C_2O_x$ composites with high specific surface area by in situ growth of TiO_2 nanowires on $Ti_3C_2T_x$ via hydrothermal and post-thermal treatment processes in a mixed solution of NaOH and H_2O_2 , while uniform -O adsorption was achieved by the surface groups of $Ti_3C_2T_x$. The morphological characteristics of $TiO_2/Ti_3C_2O_x$ are revealed through the SEM and TEM images presented in Figure 5a and 5b, respectively. X-ray photoelectron spectroscopy (XPS) revealed a notable reduction in the F 1s intensity of $TiO_2/Ti_3C_2O_x$ in comparison to $Ti_3C_2T_x$ (Figure 5d). The presence of adsorbed O and Ti-O indicates that the surface groups of the MXene of the composite after the post-annealing treatment are primarily -O (Figure 5c). A significant number of -O groups are adsorbed on the surface of $Ti_3C_2O_x$ with a high work function (4.98 eV), which can form Schottky junctions with TiO_2 and act as electron mediators in photocatalytic reactions. The number of $TiO_2/Ti_3C_2O_x$ heterojunctions is one of the major determinants for photocatalytic activity. At the interface of $TiO_2/Ti_3C_2O_x$, photogenerated electrons and holes are efficiently separated through Schottky junctions, resulting in the accumulation of electrons on $Ti_3C_2O_x$. This enrichment of electrons facilitates

the provision of active sites for the hydrogen generation reaction. The composite exhibited an exceptional photocatalytic hydrogen evolution rate of 346.8 μmol g^{-1} h^{-1}. Peng et al. [71] treated $Ti_3C_2T_x$ MXene with ethylene glycol to obtain MXene with -OH terminals on the surface, and TiO_2 heterojunctions with tunable anatase/rutile ratio were grown in-situ on it by hydrothermal oxidation route to synthesize A/R-TiO_2/$Ti_3C_2T_x$. Since photogenerated holes possess a greater effective mass than electrons and they move and migrate slower compared to photogenerated electrons, controlling the transfer kinetics of these holes can effectively improve the photocatalytic performance [72]. $Ti_3C_2T_x$ MXene with a substantial amount of -OH groups adsorbed on its surface has a low work function of 2.28 eV, enabling it to serve as an effective hole mediator in the photocatalytic reaction. During the photocatalytic hydrogen evolution reaction, photogenerated carriers are separated at the anatase/rutile heterojunction interface. Additionally, the photogenerated holes present on the TiO_2 valence band are captured by $Ti_3C_2T_x$ (T = -OH), which leads to an enhancement in charge separation efficiency. The PHE performance of A/R-TiO_2/$Ti_3C_2T_x$ reached 4672.0 μmol g^{-1} h^{-1} (0.2 wt% Pt), exhibiting an apparent quantum yield of 27.11% at 350 nm, which is significantly surpasses that of the commonly used commercial P25. In addition to TiO_2, other metal oxides in combination with MXene have also been reported in recent reports for their applications in photocatalytic hydrogen production. CeO_2, as the most common rare earth metal oxide, is widely used as an efficient photocatalyst due to its simple synthesis and excellent redox capacity [73]. Zhu et al. [74] successfully prepared 2D Ti_3C_2 MXene/3D CeO_2 photocatalysts by electrostatic interaction self-assembly and complexed ultrathin exfoliated Ti_3C_2 MXene nanosheets on the

surface of hexahedral prism-anchored octahedral CeO_2. The CeO_2/MXene sample exhibits a photocurrent intensity 1.25 times higher than that of CeO_2. Additionally, the UV-vis absorption spectrum is red-shifted and the bandgap is narrowed, indicating that the introduction of MXene not only enhances the transfer rate of photogenerated carriers but also broadens the photoresponse range of the material. The experimental results confirmed a significant enhancement in the PHE rate of CeO_2/MXene, exceeding that of CeO_2 by more than twofold. The increase in photocatalytic activity can be attributed to the formation of Schottky heterojunction between CeO_2 and Ti_3C_2, which enables the excited electrons in CeO_2 to rapidly transfer to MXene through the interfacial effect and undergo a proton reduction reaction. Consequently, charge separation is improved, and the carrier lifetime is extended. Furthermore, Zong and colleagues [75] utilized a straightforward two-phase compounding method to synthesize $Ti_3C_2T_x$-MoO_{3-x} ultrathin nanowire composite with oxygen vacancies, which demonstrated exceptional photocatalytic properties. Utilizing triethanolamine as a sacrificial agent, the photocatalytic hydrogen evolution rate reached 36.1 μmol g^{-1} h^{-1}, marking a 6-fold enhancement compared to the original material.

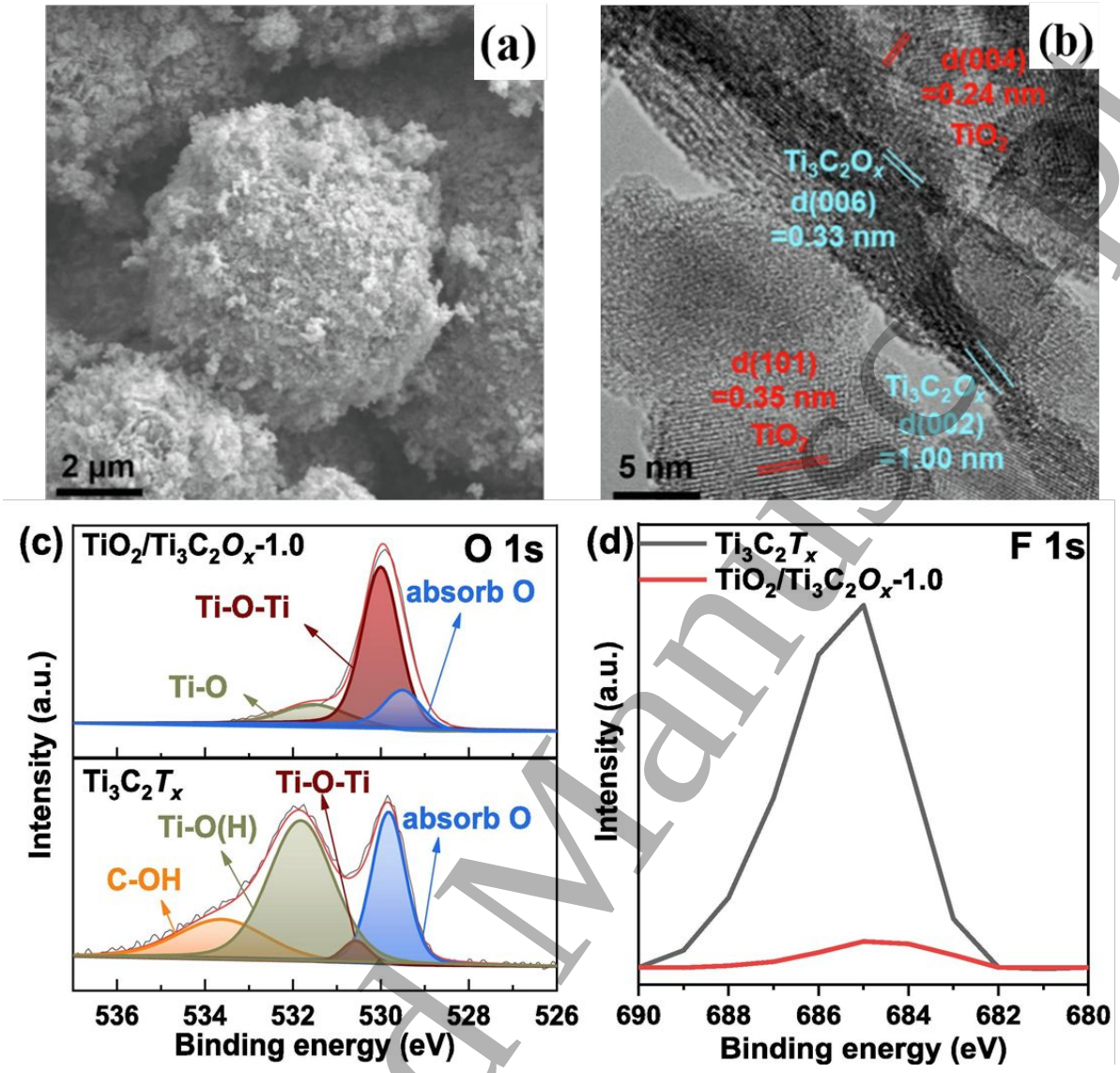

Figure 5. (a) SEM image of $TiO_2/Ti_3C_2O_x$-1.0; (b) TEM image of $TiO_2/Ti_3C_2O_x$-1.0; XPS spectra of (c) O 1s and (d) F1s of $Ti_3C_2T_x$ and $TiO_2/Ti_3C_2O_x$-1.0 [70]. Copyright 2023 Elsevier.

3.1.2 Composite with TMSS

Transition metal sulfides and selenides, which are widely available, easy to synthesize, have narrow band gaps and excellent photoresponse, are an important class of semiconductor photocatalysts [76]. Therefore, combining MXene with them to further enhance the photocatalytic activity is promising. The primary limitation in harnessing light energy for

photocatalytic reactions lies in the semiconductors' insensitivity to visible and infrared light. For example, light with wavelengths less than 500 nm cannot be absorbed by CdS. Huang et al. [78] obtained a new stable $Ti_3C_2T_x$ MXene/CdS heterojunction catalyst by utilizing a solvothermal approach to grow 2D CdS nanosheets directly on the interface of MXene. As MXene is an all-optical absorbing material with a strong near-infrared photoresponse, the created composite demonstrates outstanding light absorption properties and is able to effectively absorb energy from ultraviolet to near-infrared (UV-NIR) wavelengths, extending the light absorption range of CdS. Meanwhile, MXene can effectively convert various light energy into heat and form high-temperature active sites at the interface between CdS and MXene, which significantly improves the catalytic reaction rate. Due to the photothermal effect, the photocatalytic hydrogen evolution rate of 2D/2D $Ti_3C_2T_x$ MXene/CdS reaches 27.4 mmol g^{-1} h^{-1}, surpassing the rate of pure CdS by a factor of 4.2, under the conditions of near-infrared light irradiation and Na_2S/Na_2SO_3 as sacrificial agents. In addition to binary metal sulfides, polymetallic sulfides exhibit excellent PHE properties in photocatalytic process due to synergistic interactions between different metal ions. For example, the ternary semiconductor metal sulfide $CdIn_2S_4$ (CIS) is attracting increasing attention due to its good energy band structure, remarkable stability, and straightforward preparation process. [79]. A novel 2D/2D Ti_3C_2 MXene/$CdIn_2S_4$ (MXCIS) Schottky heterojunction photocatalyst with S vacancies was constructed by Liu et al. [82]. Experimental results reveal that the best sample, 5-MXCIS (Ti_3C_2 MXene sheets loading of 5 wt%), exhibits excellent photocatalytic hydrogen evolution performance when exposed to visible light. Specifically, its performance is nearly seven times

higher than that of the pure $CdIn_2S_4$ (CIS). However, with the further increase of Ti_3C_2 MXene sheets (MXs) content, the excessive amounts of MXs hinder the light-harvesting capability of CIS, ultimately resulting in a decline in PHE efficiency. The improved photocatalytic performance exhibited by the composites is attributed to the robust interface between Ti_3C_2 MXene and 2D CIS nanoplates that enhances the light harvesting ability and improves the charge separation rate, inhibiting the photoexcited electron-hole pair recombination. Additionally, the existence of S vacancies on the composite's surface aids in capturing free electrons, further enhancing photocatalytic efficiency. Copper-based quaternary sulfides are also an important class of metal sulfide photocatalysts in view of their fantastic visible light absorption properties and thermodynamic stability [83], and are therefore promising for compositing with MXene. Sun et al. [84] fabricated 1D/2D CuZnInS/Ti_3C_2 (1D/2D CZIS/TC) nanocomposite photocatalyst through a convenient one-pot hydrothermal method, as shown in Figure 6a. The unique 1D/2D heterojunction structure enhances the specific surface area of the complex, offering an abundance of photocatalytic active sites. Additionally, the incorporation of highly conductive Ti_3C_2 nanosheets can increase the carrier separation efficiency of CuZnInS. The combination of these two factors leads to an improvement in PHE efficiency. Under the condition of Na_2S/Na_2SO_3 as sacrificial reagents, the 13wt% 1D/2D CuZnInS/Ti_3C_2 achieves a hydrogen evolution rate of 15.34 mmol g^{-1} h^{-1}, which is 4.5 times higher than that of pure CuZnInS (Figure 6b). The composite photocatalyst exhibits an apparent quantum efficiency of 0.39% under 365 nm wavelength light irradiation and 0.24% under 420 nm, respectively (Figure 6c). The AQE results verified that 13 wt%-CZIS/TC have efficient

ultraviolet and visible light absorption.

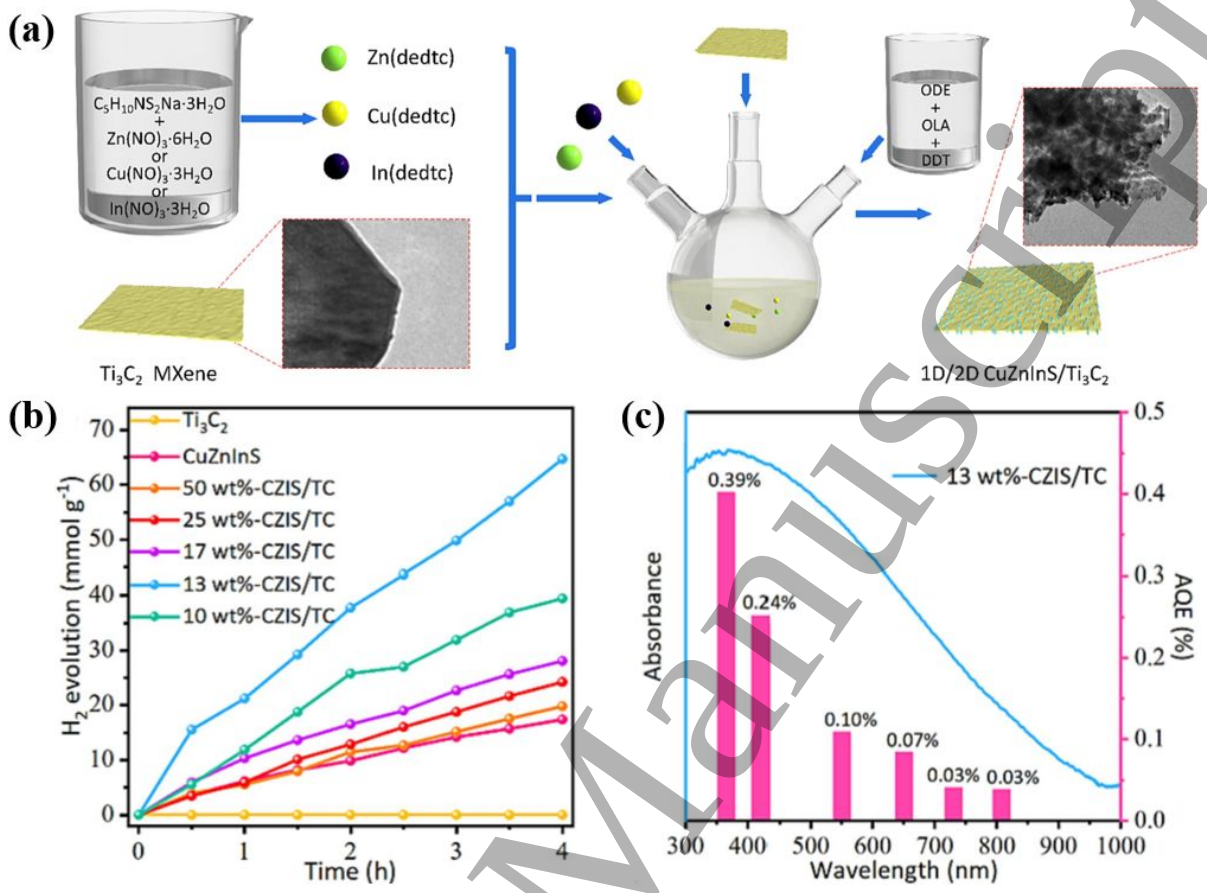

Figure 6. (a) The schematic illustration of the preparation process of 1D/2D CuZnInS/Ti_3C_2; (b) Time-yield PHE curves of samples; (c) wavelength dependent AQEs of 13 wt%-CZIS/TC [84]. Copyright 2024 Elsevier.

Our group has also conducted relevant studies on the composites of transition metal sulfides and selenides with MXene for photocatalytic hydrogen production applications, clearly revealing and elucidating the microstructures and photocatalytic working mechanisms of these catalysts. Firstly, Ti_3C_2 MXene nanosheets were synthesized by LiF-HCl method, and then $Cd_{0.5}Zn_{0.5}S$ and Ti_3C_2 MXene binary heterojunction photocatalysts were obtained by in-situ hydrothermal method [85]. At the same time, the microscopic morphology and

photoelectrochemical properties of the catalyst are characterized. Figure 7 (a-d) shows the TEM and high-resolution TEM (HRTEM) images of $Cd_{0.5}Zn_{0.5}S$, Ti_3C_2 MXene, and $Ti_3C_2/Cd_{0.5}Zn_{0.5}S$ composites, respectively. As can be observed, $Cd_{0.5}Zn_{0.5}S$ exists in the form of nanorods, while MXene exhibits a two-dimensional nanosheet morphology, illustrating the successful preparation of the composites. In addition, the electron transfer mechanism during photocatalytic water decomposition was investigated by in situ XPS. As illustrated in Figure 7 (e-h), the binding energies of the Cd 3d, Zn 2p and S 2p peaks exhibited a positive shift under light conditions in comparison to dark conditions. Conversely, the Ti 2p peak demonstrated a negative shift. The above results indicate that electrons are transferred from $Cd_{0.5}Zn_{0.5}S$ to Ti_3C_2 nanosheets to catalyze the reduction of adsorbed H^+ to H_2 during the photocatalytic process.

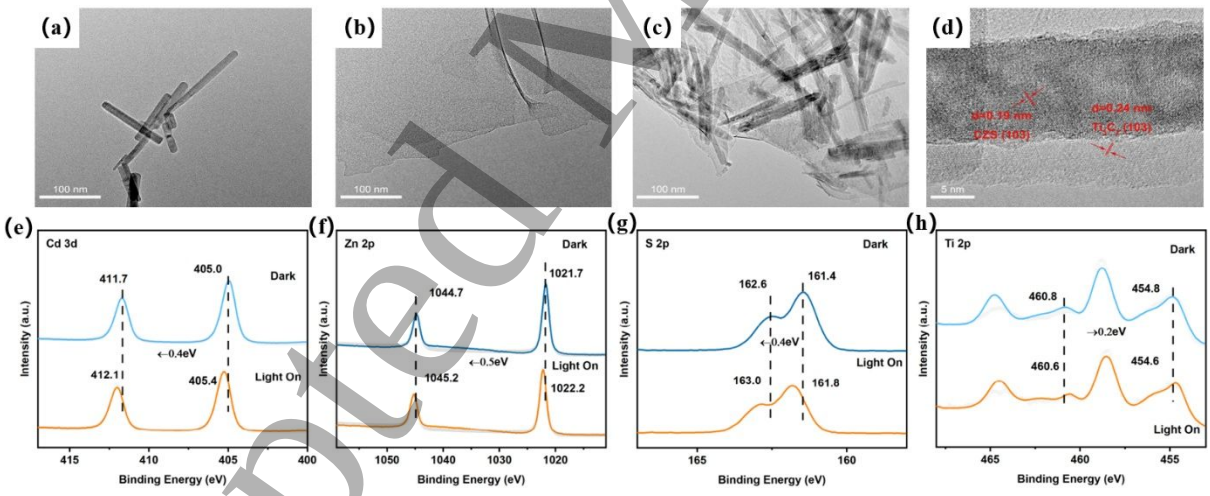

Figure 7. TEM images of (a) $Cd_{0.5}Zn_{0.5}S$, (b) Ti_3C_2 MXene, (c) $0.5Ti_3C_2/Cd_{0.5}Zn_{0.5}S$, (d) HRTEM image of $0.5Ti_3C_2/Cd_{0.5}Zn_{0.5}S$ and high-resolution in situ XPS spectra of Cd 3d (e), Zn 2p (f) S 2p (g), and Ti 2p (h) of $Ti_3C_2/Cd_{0.5}Zn_{0.5}S$ [85].

We have also investigated the photocatalytic hydrogen evolution properties of the

transition metal selenide CdSe composited with Ti_3C_2 MXene [86]. The TEM image (**Figure 8**a) demonstrates that CdSe is loaded on Ti_3C_2 nanosheets in the form of nanorods, and the lattice stripes of CdSe and Ti_3C_2 as well as the existence of close interfacial contacts between CdSe and MXene can be observed by HRTEM (**Figure 8**b), confirming the successful synthesis of CdSe-MXene composites. The photocatalytic hydrogen evolution performance of CdSe-MXene composites are presented in **Figure 8**c. Notably, the 10%MX-CdSe sample exhibits the highest photoactivity, achieving a hydrogen production rate of 763.2 μmol g^{-1} h^{-1}, which is six times higher than that of the bare CdSe sample. Furthermore, the hydrogen production activity test of CdSe-10%MX remained highly active after five cycles, indicating its excellent catalytic stability in photocatalytic cycling tests (Figure 8d).

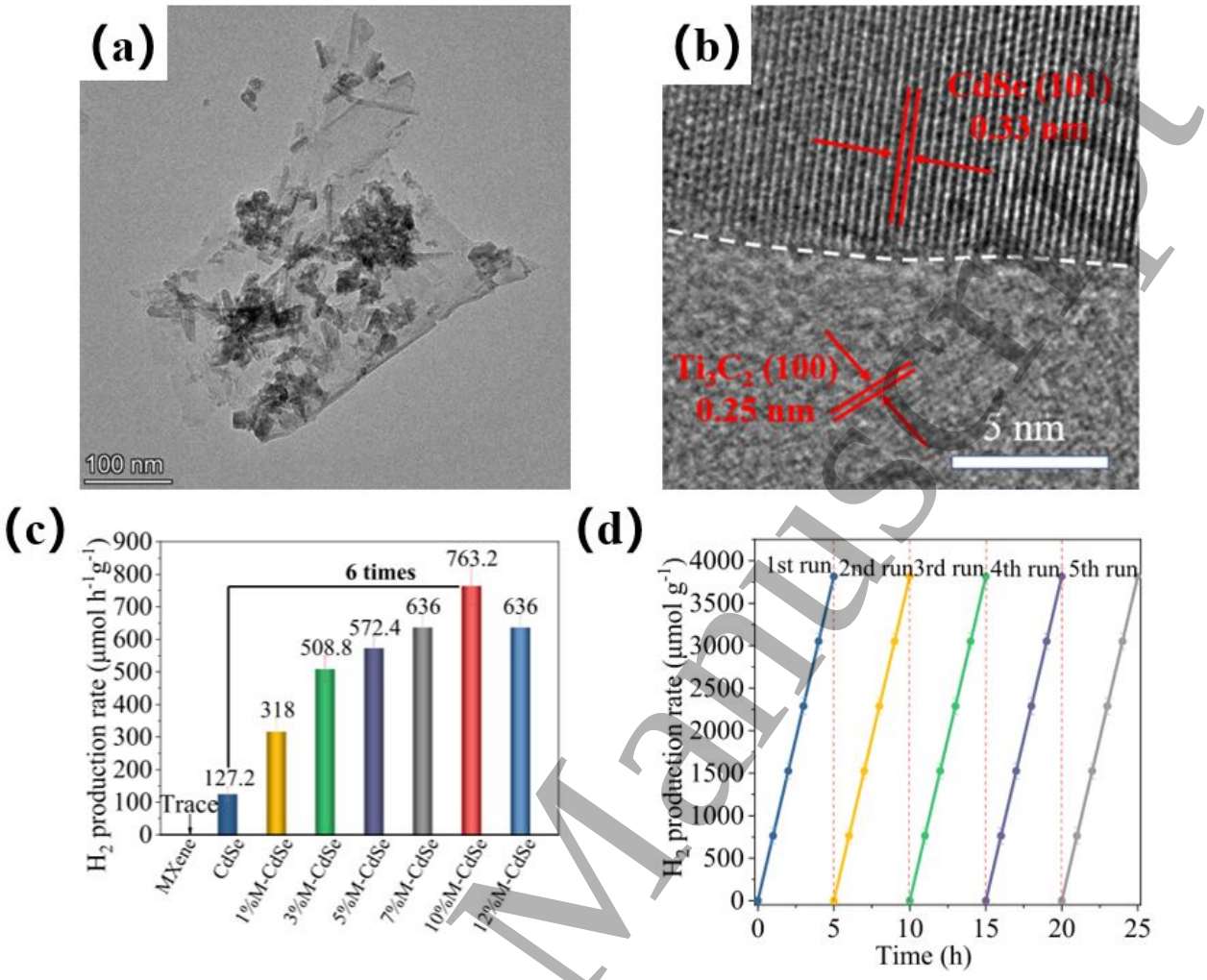

Figure 8. (a) TEM image of CdSe-MXene, (b) HRTEM image of CdSe-MXene, (c) Photocatalytic activity of H_2 production over x-MXene/CdSe (x = 0, 1%, 3%, 5%, 7%, 10%, 12% and 100%) hybrids, (d) Recycling photocatalytic H_2 production tests over CdSe-MXene composite [86]. Copyright 2023 Elsevier.

3.1.2 Composite with g-C_3N_4

Graphite-like phase carbon nitride (g-C_3N_4) is a new kind of semiconductor material with a stable layered structure similar to graphite, which is inexpensive and easy to synthesize. In 2009, Wang et al. [87] reported the first use of g-C_3N_4 to produce hydrogen by photolysis of

water under visible light irradiation, which quickly attracted widespread attention from the scientific community. However, conventional g-C_3N_4 suffers from defects such as small specific surface area, low utilisation of sunlight and high electron-hole recombination rate, which limit its photocatalytic performance, and its catalytic performance can be significantly improved by composite modification with MXene. A protonated graphitic carbon nitride (PCN)/Ti_3C_2 MXene heterojunction, characterized by robust interfacial interactions, has been synthesized by Xu et al. [88]. By protonation, pre-treatment of nanostructured g-C_3N_4 with hydrochloric acid transforms the negative charges on its surface to positive ones, adjusting the band gap and ionic conductivity, thereby enhancing light absorption. The photocatalytic hydrogen production efficiency of the sample loaded with 20 mg of MXene can reach 2181 μmol g^{-1}, which is 5.5 and 2.7 times higher than that of pure g-C_3N_4 and protonated g-C_3N_4 (PCN), respectively. The excellent hydrogen evolution performance exhibited by the composite photocatalysts can be ascribed to the charge-modulated surface of PCN, as well as the enhanced charge transport at the 2D/2D PCN/Ti_3C_2 MXene Schottky heterojunction interface. Additionally, one-dimensional (1D) g-C_3N_4 nanotubes exhibit exceptional visible-light photocatalytic activity, stemming from their distinctive 1D structure, low mass-transfer resistance, short reactant diffusion distances, excellent light trapping capability, and efficient carrier transport. Huang et al. [89] successfully synthesized P-doped tubular g-C_3N_4 (PTCN) through phosphorus acid-assisted hydrothermal heating and calcination, and then modified PTCN by electrostatic self-assembly with layered 2D Ti_3C_2 MXene nanosheets to obtain P-doped tubular g-C_3N_4/Ti_3C_2-MXene (PTCN/TC) composites. After doping with P, impurity

energy levels are introduced, which shift the g-C_3N_4 conduction band edges to more positive positions and narrow the band gap, thus enhancing the light absorption, while the 1D structure is able to significantly facilitate the separation of photogenerated carriers. Ti_3C_2 possesses numerous hydrophilic functional groups on its surface, which facilitate robust interactions with water molecules, allowing it to act as a co-catalyst and a fast electron transfer channel. Furthermore, the built-in electric field that forms between the 1D/2D g-C_3N_4/Ti_3C_2 Schottky heterojunctions can inhibit photogenerated carriers from recombining through the Schottky barrier and enhance the photocatalytic activity of the composite. The optimized P-doped tubular g-C_3N_4/Ti_3C_2 composite achieved the highest hydrogen evolution rate of 565 μmol g^{-1} h^{-1} when methanol was used as a sacrificial agent. Vanadium-based MXene (V_2C) has also received much attention because of its multiple oxidation states and thinner structure compared to the most widely studied Ti_3C_2, which can provide a larger specific surface area for photon absorption and facilitate the photocatalytic process. As mentioned above, Sherryna et al. [38] prepared well-structured V_2C MXene coupled g-C_3N_4 2D/2D nanohybrids through physical mixing. In the water-methanol sacrificial reagent, the photocatalytic activity dropped in the third cycle of testing, which was attributed to the homolytic decomposition of g-C_3N_4 under the presence of light. Instead, the hydrogen production rate of the water-TEOA system remained stable over several hours of cycling. The experimental results and characterizations demonstrate that the accumulation of holes drives the homocleavage of g-C_3N_4 functional groups during the photocatalytic reaction, and triethanolamine (TEOA) can be used as a hole scavenger to slow down the decomposition of g-C_3N_4, thereby aiding in maintaining the

composite's stable photocatalytic activity in a continuous cycle. Meanwhile, V_2C acts as an electron trapper and effectively promotes the separation of photogenerated carriers. The PHE rate of the sample with 15 wt% V_2C loading can reach 360 μmol g^{-1} h^{-1}, which is 4.23 times higher than that of pure g-C_3N_4. Various forms of MXene have been derived from the 2D MXene, including nanotubes, nanoscrolls, and quantum dots [90]. The MXene quantum dots (QDs) possess not only the exceptional physicochemical properties inherent to the original MXene but also exhibit swift ion transport, prompt electron delivery to the active site, environmental friendliness, and an intrinsic structure with rich surface chemistry. Compared to conventional monometallic MXene, bimetallic MXene quantum dots offer superior conductivity and broader structural modulation. Ding et al. [91] synthesized 0D/2D bimetallic $Mo_2Ti_2C_3$ QDs/g-C_3N_4 heterojunction by electrostatic self-assembly strategy (Figure 9a). $Mo_2Ti_2C_3$ quantum dots modified g-C_3N_4 can regulate its electronic structure and promote the formation of an interfacial electric field, which drives the spatial segregation and transfer of charges and prolongs the lifetimes of the excited states of the charges. At the same time, the interfacial effect of the 0D/2D heterojunction reduces the light-induced compounding of electrons and holes, improves charge utilization and therefore enhances the photocatalytic activity of the material. $Mo_2Ti_2C_3$ QDs/g-C_3N_4 exhibits excellent and consistent PHE rate of up to 2809 μmol g^{-1} h^{-1}, which is 7.96 times higher than that of pristine g-C_3N_4 nanosheets (Figure 9b), while its apparent quantum efficiency at 420 nm wavelength reaches 3.8% (Figure 9c), indicating that the composite has a superior absorption in the visible light region and is able to utilise photons at this wavelength more efficiently.

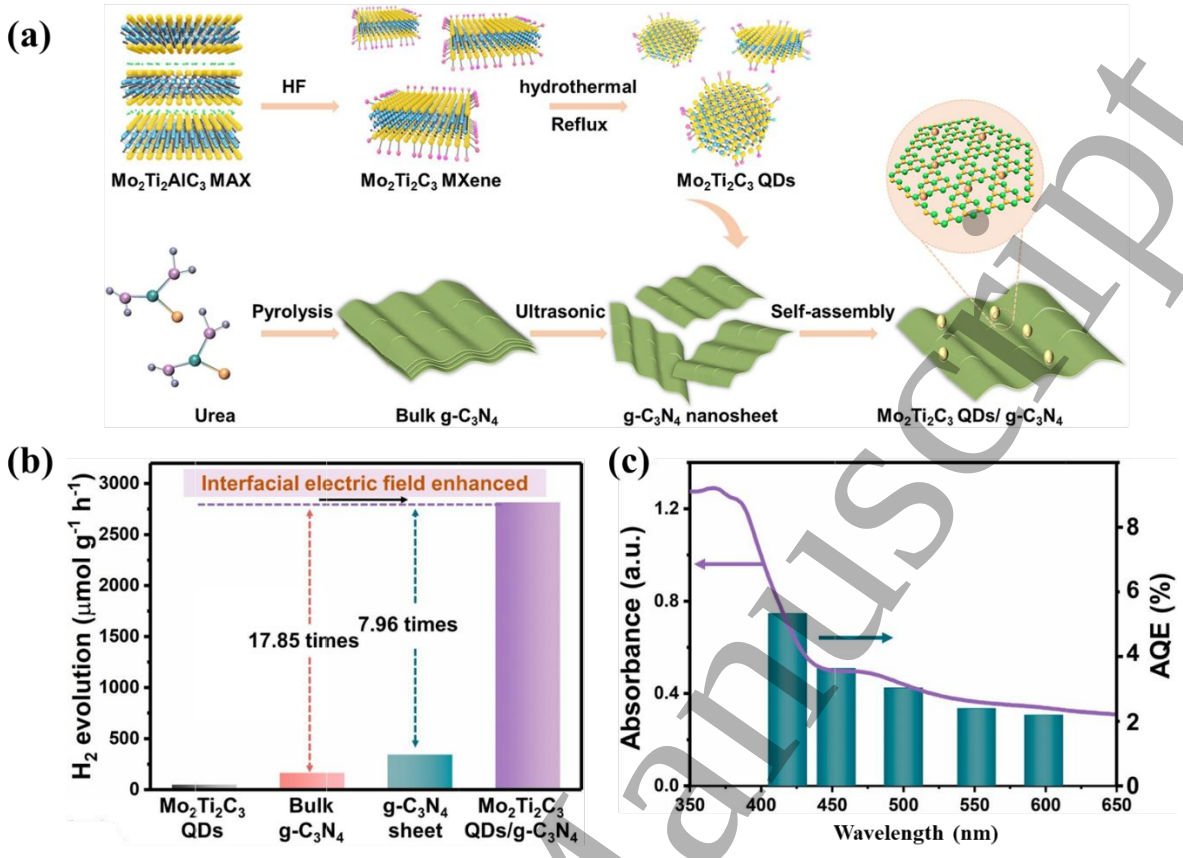

Figure 9. (a) Schematic diagram of the preparation procedure for $Mo_2Ti_2C_3$ QDs/g-C_3N_4; (b) The PHE activity of various samples; (c) UV–visible diffuse reflectance spectroscopy and the AQEs of $Mo_2Ti_2C_3$ QDs/g-C_3N_4 [91]. Copyright 2024 Elsevier.

3.1.3 Composite with organics

Inorganic-organic hybrid photocatalysts combine the strengths of their inorganic and organic components. The inorganic component retains its high intensity, narrow band gap, and excellent optical properties, while the organic component maintains its low cost, high absorption coefficient, and vast specific surface area. Furthermore, the synergistic interaction between these two components generates novel interfacial properties, leading to the further enhancement of photocatalytic activity. As a result, these composites represent a promising

class of materials [92]. Organic materials such as natural pigments and organic dyes with low cost and high light absorption coefficients can exhibit outstanding photocatalytic activity when compounded with MXene. Bacteriochlorophyll (BChl), a photosynthetically active pigment abundant in bacteria and vital for photosynthesis, has been extensively employed in artificial photosynthesis research. Its exceptional ability to efficiently absorb solar energy and convert it into chemical energy makes it a highly desirable candidate in this field. Li et al. [93] prepared five distinct BChl-a derivatives, each featuring unique esterified side chains on the C17 substituent, through a solvent evaporation process and deposited them on the surface of $Ti_3C_2T_x$ MXene to synthesize BChl-n@$Ti_3C_2T_x$ (n=1~5) composite photocatalysts. Raman spectra show that the I_D/I_G value of BChl-5@$Ti_3C_2T_x$ is increased compared to that of pristine $Ti_3C_2T_x$ (Figure 10a), indicating that there are more structural defects in the graphitized carbon, which facilitates the efficient transfer of electrons from BChl-5 to $Ti_3C_2T_x$. Meanwhile, BChl-5 has good self-aggregation properties so that it can achieve high photocapture efficiency as a photosensitizer. Of all the BChl-n@$Ti_3C_2T_x$ (n=1~5) composites, BChl-5 with a quaternary ammonium terminal exhibited the most impressive PHE performance of 51 μmol g^{-1} h^{-1} under visible and near-infrared light irradiation conditions using ascorbic acid (AA) as a sacrificial agent. Squaraine (SQ) dyes, a notable class of organic functional dyes, have gained widespread application in artificial photosynthesis due to their strong absorption and emission properties in the visible and near-infrared regions and the excellent photochemical stability [94]. A series of 2,4-bis[4-(N,N-dibutylamino)phenyl] squaraine (SQ) derivatives with a distinct number of hydroxyl groups were hybridized with $Ti_3C_2T_x$ MXene nanosheets for the first time for the

photocatalytic hydrogen production by Liu et al. [95]. In this case, SQ aggregates exhibited a uniform distribution and were securely adhered to the 2D $Ti_3C_2T_x$ MXene surface and intercalation layers (Figure 10b). The presence of four -OH functional groups in 2,4-bis[4-(N,N-dibutylamino)-2,6-dihydroxyphenyl] squaraine (SQ-3) allows it to form CT-J aggregates on the surface of $Ti_3C_2T_x$ MXene, and the extension of the distances between the electrons and holes in the large self-polymer leads to more efficient separation of electron-hole pairs , thus inhibiting their complexation, while the SQ dyes' excellent light trapping ability and the sufficient active sites provided by $Ti_3C_2T_x$ make SQ-3@$Ti_3C_2T_x$ with a mass ratio of 4 wt% exhibit the highest PHE rate of 28.6 μmol g^{-1} h^{-1}.

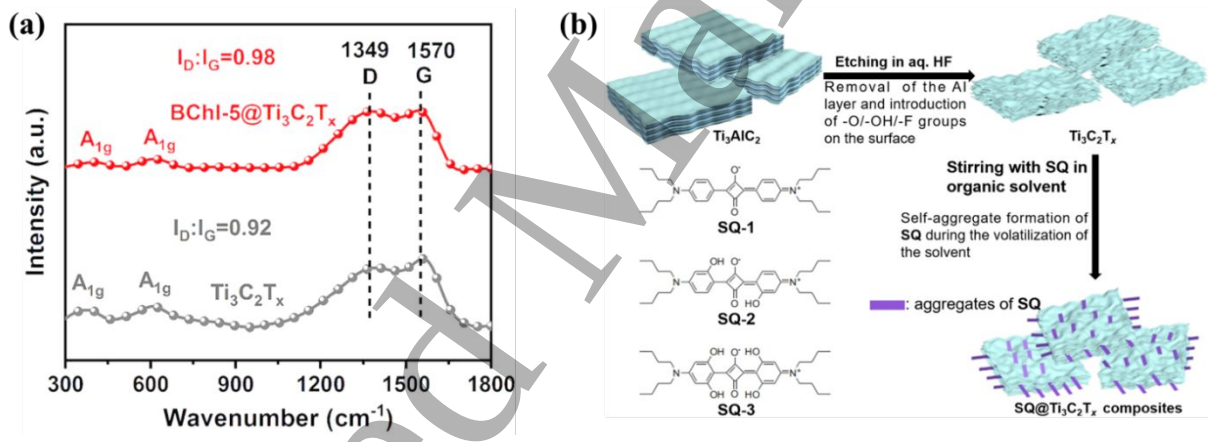

Figure 10. (a) Raman spectra of raw $Ti_3C_2T_x$ materials and BChl-5@$Ti_3C_2T_x$ composites [93]. Copyright 2024 Elsevier; (b) Chemical structures of squaraine dyes SQs-1–3 and schematic illustration of the preparation process of SQ@$Ti_3C_2T_x$ composites [95]. Copyright 2023 Elsevier.

3.2 Ternary composites

On the basis of binary complexes, the enhancement of the photocatalytic hydrogen

production performance of pristine semiconductors through synergistic interactions between the components of MXene-based ternary composites has also captured extensive attention from researchers. For instance, Wu et al. [96] first prepared MoS_2/Ti_3C_2 composites by directly reducing $(NH_4)_2MoS_4$ at the positions of 2D Ti_3C_2 MXene's reduced Ti vacancies and then grow CdS in-situ on the surface to construct ternary $CdS@MoS_2/Ti_3C_2$ (CTM) nanocomposites with close contact interfaces. In the ternary composite CTM, MoS_2 and Ti_3C_2 acted as dual co-catalysts, which made the photogenerated holes and electrons on the surface of CdS quickly transfer to Ti_3C_2 and MoS_2, respectively, as shown in Figure 11. This improved the electron-hole separation efficiency, overcomed the aggregation of pure CdS nanoparticles, and simultaneously safeguarded against the photocorrosion of CdS, which contributed to the higher photochemical stability of the composites. The synergistic interaction between Ti_3C_2 MXene and MoS_2, with lactic acid as a sacrificial agent, allowed the optimized sample to exhibit a hydrogen production rate of 14.88 mmol g^{-1} h^{-1}, which is 2.4 and 3.9 times higher than that of binary $CdS@Ti_3C_2$ and CdS/MoS_2, respectively. Chen et al. [97] designed ternary $CdS@Nb_2O_5/Nb_2CT_x$ photocatalysts with 0D/1D/2D hierarchical structures using a hydrothermal method, in which Nb_2O_5 nanorods (NRs) were derived from the in-situ oxidation of Nb_2CT_x and the CdS nanoparticles were tightly attached to Nb_2O_5/Nb_2CT_x. The synergistic effect arising from the S-scheme heterojunction between CdS and Nb_2O_5/Nb_2CT_x and the Schottky barrier between Nb_2CT_x/semiconductors leads to a remarkable enhancement of the photocatalytic activity, so that the sample 0.5 $CdS@Nb_2O_5/ Nb_2CT_x$ shows a PHE performance which is 10.3 and 7.7 times higher than that of binary $0.5CdS@Nb_2CT_x$ and $0.5CdS@Nb_2O_5$,

respectively. There is also a range of MXene-based ternary composites such as $PtO@Ti_3C_2/TiO_2$ [98], Ti_3C_2-CdS/WO_3 [99], $Ru/Nb_2O_5@Nb_2C$ [100], Ti_3C_2-$ZnIn_2S_4$-$NiSe_2$ [101], $In_2S_3/Nb_2O_5/Nb_2C$ [102], $Ti_3C_2/ZnIn_2S_4$/CdS [103] and so on. Compared to binary complexes, ternary composite photocatalysts exhibit a synergistic effect among their components that not only prevents the autoxidation and photocorrosion of semiconductors but also fosters the separation of photogenerated carriers, thus leading to an enhanced photocatalytic performance of the materials.

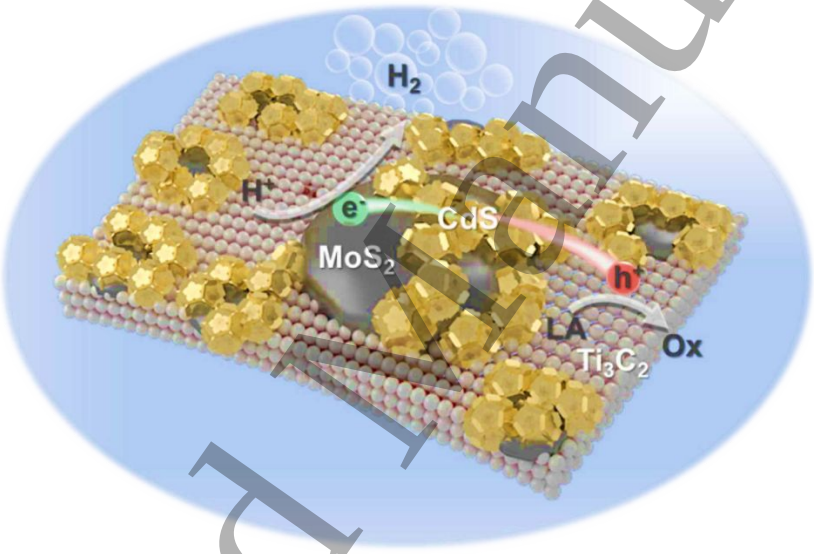

Figure 11. Proposed mechanism of charge transfer over ternary $CdS@MoS_2/Ti_3C_2$ photocatalysts during photocatalytic H_2 evolution, where LA refers to lactic acid as the sacrificial agent [96]. Copyright 2023 Elsevier.

4. Conclusion and perspective

In conclusion, MXene materials are popular co-catalysts in photocatalysis attributed to their unique structure, hydrophilicity, and excellent photovoltaic characteristics. This review

summarizes several common methods for synthesising MXene-based composites, encompassing physical mixing, electrostatic self-assembly and in-situ hydrothermal/solvothermal synthesis, and compares their advantages and disadvantages with examples. Meanwhile, some new MXene-based composite photocatalysts in the field of PHE in recent years are highlighted according to semiconductor types. Typically, in the PHE reaction, a Schottky heterojunction is formed between the semiconductor and the MXene, which mainly acts as an electron trapper, providing numerous reactive sites and facilitating the separation of photogenerated electrons and holes, thus enabling the composite to exhibit a higher hydrogen production rate than the pristine semiconductor (Table 1).

Table 1. The photocatalytic hydrogen evolution performance of MXene-based composites.

Materials	**Synthesis Methods**	**Sacrificial Regent**	**Light Source**	**H_2 Production rate ($\mu mol\ g^{-1}\ h^{-1}$)**	**Ref.**
V_2C/g-C_3N_4	Physical mixing	Methanol	35 W Xe HID lamp	360	[38]
Ti_3C_2 QD/PGCN	Electrostatic self-assembly	Triethanolamine	300 W Xe lamp	4040.95	[40]
a-TiO_2/H-TiO_2/Ti_3C_2	Electrostatic self-assembly	methanol	300 W Xe lamp	387	[41]
CdS@Ti_3C_2	Hydrothermal	Triethanolamine	300 W Xe lamp	3176.5	[43]
$ZnIn_2S_4$/Ti_3C_2 (UZNs-MNs-UZNs)	Hydrothermal	Triethanolamine	300 W Xe lamp	3475	[44]

$SrTiO_3/Ti_3C_2$	Hydrothermal	Methanol	300 W Xe lamp	344.1	[45]
$TiO_2/Ti_3C_2O_x$	Hydrothermal	Methanol	300 W Xe lamp	346.8	[70]
A/R-$TiO_2/Ti_3C_2T_x$	Hydrothermal	Methanol	300 W Xe lamp	4672	[71]
$CeO_2/Ti_3C_2T_x$	Electrostatic self-assembly	Triethanolamine	300 W Xe lamp	454.32	[74]
$Ti_3C_2T_x$-MoO_{3-x}	Two-phase assembling	Triethanolamine	300 W Xe lamp	36.1	[75]
$Ti_3C_2T_x/CdS$	Solvothermal	Na_2S/Na_2SO_3	300 W Xe lamp	27400	[78]
$Ti_3C_2/CdIn_2S_4$	Solvothermal	Na_2S/Na_2SO_3	300 W Xe lamp	180	[82]
$CuZnInS/Ti_3C_2$	Hydrothermal	Na_2S/Na_2SO_3	300 W Xe lamp	15340	[84]
$Ti_3C_2/Cd_{0.5}Zn_{0.5}S$	Hydrothermal	Na_2S/Na_2SO_3	300 W Xe lamp	15560	[85]
$CdSe@Ti_3C_2$	Hydrothermal	Na_2S/Na_2SO_3	300 W Xe lamp	763.2	[86]
Protonated g-C_3N_4 (PCN)/ Ti_3C_2	Physical mixing	Triethanolamine	300 W Xe lamp	727	[88]
P-doped tubular g-C_3N_4 (PTCN)/Ti_3C_2	Electrostatic self-assembly	Methanol	300 W Xe lamp	565	[89]
$Mo_2Ti_2C_3$ QDs/g-C_3N_4	Electrostatic self-assembly	Triethanolamine	300 W Xe lamp	2809	[91]
BChl-n@$Ti_3C_2T_x$	Solvent evaporation	Ascorbic acid	300 W Xe lamp	51	[93]
SQ@$Ti_3C_2T_x$	Physical mixing	Ascorbic acid	300 W Xe lamp	28.6	[95]
$CdS@MoS_2/Ti_3C_2$	Microwave-	Lactic acid	300 W Xe lamp	14880	[96]

	hydrothermal				
$CdS@Nb_2O_5/Nb_2CT_x$	Hydrothermal	Lactic acid	300 W Xe lamp	2715.8	[97]

In addition, although current research into the synthesis and application of MXene-based composites is extensive, there remain certain limitations that can be further improved in the future:

1. As of now, the predominant technique for synthesizing MXene involves the etching of the MAX phase using hydrofluoric acid (HF). This method demonstrates remarkable efficacy in the rapid removal of the A-layer from the MAX phase, rendering it applicable across a diverse array of MXene precursors. Despite its broad applicability and efficiency, the synthesis process is marred by the highly corrosive nature of HF, which poses significant risks to both safety and environmental integrity. Although the environmental repercussions associated with the use of HF can be somewhat alleviated through employing a mixed solution of acid and fluoride, challenges persist in the subsequent phases of product washing and waste management, highlighting substantial areas for improvement. In pursuit of safer alternatives, researchers have explored various non-fluoride etching techniques such as the molten salt method and chemical vapor phase deposition. However, these methods suffer from limitations including stringent operational conditions and disappointingly low yields of MXene, which hinder their scalability and practical application. More recently, gas-phase selective etching has emerged as a promising technique, capable of directly yielding multilayer MXene powders without necessitating the removal of etchants and by-products. Nonetheless, this method still requires

a supplementary delamination process to achieve single-layer MXene, which adds complexity to the synthesis. Given these considerations, there is a pressing need for the development of novel synthesis strategies that are not only devoid of fluorine but also cost-effective and uncomplicated. Future research should focus on refining these methods to enhance their feasibility and environmental sustainability, thereby broadening the scope and applicability of MXene materials in the field of photocatalytic hydrogen production;

2. $Ti_3C_2T_x$ remains the most widely used MXene; however, other MXenes such as V_2CT_x, Nb_2CT_x, and Mo_2CT_x have not been sufficiently explored in the context of photocatalytic hydrogen production. While $Ti_3C_2T_x$ demonstrates excellent performance in photocatalytic applications, it is crucial to investigate the potential of these less-studied MXene materials. These materials may possess unique electronic structures and surface chemical properties that could offer advantages over $Ti_3C_2T_x$ in photocatalytic hydrogen production. Furthermore, the 2D transition metal borides (MBene) and transition metal carbo-chalcogenides (TMCC) derived from MXenes have not been extensively studied as co-catalysts in the field of photocatalytic hydrogen production. Specifically, TMCC stand out as promising candidates due to their tunable bandgaps, high carrier mobility, and robust light-matter interactions. These characteristics render TMCC highly conducive for applications in photocatalytic hydrogen production. Therefore, a comprehensive investigation of these underexplored MXenes and their derivatives could reveal novel avenues for the optimization and advancement of photocatalytic hydrogen production technologies;

3. The surface terminations of MXene significantly influence its electronic structure and

surface chemical environment, thereby affecting its photocatalytic activity. Typically, MXene obtained via solution-based etching features terminations such as -OH, -O, -F, and -Cl, with their proportions adjustable to some extent by the concentration of HF used during synthesis. Among these, -OH groups enhance MXene's hydrophilicity, facilitating the adsorption of reactants, while -O groups increase surface electron density, aiding in the migration and separation of photogenerated electrons and holes. In addition to these common terminations, alternative processing techniques can produce terminations like -NH, -S, and -Se. However, research on MXene with these novel terminations in photocatalysis remains limited. It has also been observed that MXene subjected to high-temperature H_2 treatment can produce termination-free MXene (MX), with the exposed surface exhibiting higher catalytic activity. In conclusion, studying and optimizing the various surface terminations of MXene is crucial for its application in photocatalysis. By fine-tuning these terminations, we can develop highly efficient MXene-based composites for applications in photocatalytic hydrogen production. Future research should focus on exploring terminations above or new terminations and understanding their impact on the photocatalytic properties of MXene to fully harness its potential in sustainable energy and environmental applications.

4. MXenes are prone to oxidation and structural degradation over time, which can compromise their performance. MXenes are highly susceptible to oxidation when exposed to air. Oxygen molecules interact with the surface of MXene, leading to the formation of metal oxides and hydroxides. In aqueous environments, MXenes can undergo oxidation due to dissolved oxygen, leading to the formation of surface oxides and hydroxides. Additionally, MXenes can

hydrolyze in the presence of water or moisture. This process breaks down the material, resulting in the formation of metal hydroxides and potentially releasing metal ions into the solution. The rate of hydrolysis can be influenced by the pH of the environment. Acidic or basic conditions can accelerate the degradation process. To ensure long-term stability of MXene materials, regulating the MAX phase structure and the MXene etching process can produce MXene materials with fewer surface defects and larger layer sizes, effectively delaying oxidation. From the point of view of storage, it is crucial to control storage conditions, avoiding moisture and high temperatures to minimize oxidation and degradation. Developing new methods to enhance the oxidation resistance of MXene, such as partial or complete oxidation to create MXene oxide derivatives, can improve stability. Controlling the oxidation process of MXene can also construct MXene/metal oxide heterostructures, potentially exhibiting superior photocatalytic performance.

Declaration of Competing Interest

The authors declare that they have no known competing financial interests or personal relationships that could have appeared to influence the work reported in this paper.

Acknowledgments

This work was financially supported by the National Key Research and Development Program of China (2021YFA1501404), Natural Science Foundation of Shanghai (22ZR1404200), and Natural Science Foundation of Shanghai Science and Technology Committee (19DZ2270100).

References

[1] R. Kawamura, N.T. Cuong, T. Fujita, R. Ishibiki, T. Hirabayashi, A. Yamaguchi, I. Matsuda, S. Okada, T. Kondo and M. Miyauchi 2019 *Nat. Commun.* **10** 4880.

[2] Y. Guo, Q. Zhou, J. Nan, W. Shi, F. Cui and Y. Zhu 2022 *Nat. Commun.* **13** 2067.

[3] D. Gao, J. Xu, L. Wang, B. Zhu, H. Yu and J. Yu 2021 *Adv. Mater.* **34** 2108475.

[4] Y. AlSalka, A. Hakki, J. Schneider and D.W. Bahnemann 2018 *Appl.Catal. B* **238** 422.

[5] B.X. Zhou, S.S. Ding, K.X. Yang, J. Zhang, G.F. Huang, A. Pan, W. Hu, K. Li and W.Q. Huang, 2021 *Adv. Funct. Mater.* **31** 2009230.

[6] H.H. Zhang, H.J. Gu, X.H. Wang, L.F. Li, J.H. Zhang, S.Y. Chang and W.-L. Dai, 2022 **622** 539.

[7] W. Shi, M. Li, X. Huang, H. Ren, C. Yan and F. Guo 2020 *Chem. Eng. J.* **382**, 122960.

[8] A. Mishra, A. Mehta, S. Basu, N.P. Shetti, K.R. Reddy and T.M. Aminabhavi 2019 *Carbon* **149** 693.

[9] L.F. Li, X.H. Wang, H.J. Gu, H.H. Zhang, J.H. Zhang, Q. Zhang and W.-L. Dai 2022 *Inorg. Chem.* **61** 4760.

[10] S.Y. Chang, H.J. Gu, H.H. Zhang, X.L. Wang, Q. Li, Y.Y. Cui and W.-L. Dai 2023 *J Colloid Interf Sci* **644** 304.

[11] H.H. Zhang, H.J. Gu, X.L. Wang, S.Y. Chang, Q. Li and W.-L. Dai 2023 *Chem. Eng. J* **457** 141185.

[12] B. Mahler, V. Hoepfner, K. Liao and G.A. Ozin 2014 *J. Am. Chem. Soc.* **136** 14121.

[13] Y.Q. Tang, C.H. Mak, R.G. Liu, Z.K. Wang, L. Ji, H.S. Song, C.Y. Tan, F. Barrière and H.Y. Hsu, 2020 *Adv. Funct. Mater.* **30** 2070343.

[14] B. Allured, S. DelaCruz, T. Darling, M.N. Huda and V. Subramanian 2014 *Appl.Catal. B* **144** 261.

[15] L. Xu, W.Q. Chen, S.Q. Ke, S.M. Zhang, M. Zhu, Y. Zhang, W.Y. Shi, S. Horike and L. Tang 2020 *Chem. Eng. J* **382** 122810.

[16] R. Shen, X. Li, C. Qin, P. Zhang and X. Li 2023 *Adv. Energy Mater.* **13** 2203695.

[17] Z.P. Li, T.Q. Deng, S. Ma, Z.W. Zhang, G. Wu, J.A. Wang, Q.Z. Li, H. Xia, S.W. Yang, and X.M. Liu 2023 *J. Am. Chem. Soc.* **145** 8364.

[18] Y.X. Chen, X. Luo, J.J. Zhang, L. Hu, T. Xu, W. Li, L. Chen, M. Shen, S.B. Ren, D.M. Han, G.H. Ning and D. Li 2022 *J. Mater. Chem. A* **10** 24620.

[19] Q. Zhang, H.J. Gu, X.H. Wang, L.F. Li, J.H. Zhang, H.H. Zhang, Y.-F. Li, W.-L. Dai 2021 *Appl. Catal. B* **298** 120632.

[20] J.J. Duan, S. Chen and C. Zhao 2017 *Nat. Commun.* **8** 15341.

[21] Y.P. Zhu, J. Yin, E. Abou-Hamad, X. Liu, W. Chen and T. Yao, O. F. 2020 *Adv. Mater.* **32** 1906368.

[22] S.C. Sun, Y.C. Zhang, G.Q. Shen, Y.T. Wang, X.L. Liu, Z.W. Duan, L. Pan, X.W. Zhang and J.J. Zou 2019 *Appl. Catal. B* **243** 253.

[23] X.L. Li, G.Q. Yang, S.S. Li, N. Xiao, N. Li, Y.Q. Gao, D. Lv and L. Ge 2020 *Chem. Eng. J* **379** 122350.

[24] F.F. Chen, C.Y. Wu, J.N. Wang, C.P. Francois-Xavier and T. Wintgens 2019 *Appl.Catal. B* **250** 31.

[25] T. Yoshinaga, M. Saruyama, A. Xiong, Y. Ham, Y.B. Kuang, R. Niishiro, S. Akiyama, M. Sakamoto, T.Hisatomi, K. Domen and T. Teranishi 2018 *Nanoscale* **10** 10420.

[26] M. Naguib, M. Kurtoglu, V. Presser, J. Lu, J. Niu, M. Heon, L. Hultman, Y. Gogotsi and

M.W. Barsoum 2011 *Adv. Mater.* **23** 4207.

[27] J. Sun, B. Liu, Q. Zhao, C. H. Kirk and J. Wang 2023 *Adv. Mater.* 35 2306072.

[28] B. S. Reghunath, S. Rajasekaran, S. Mathew, D. Pinheiro, S. Devi K. R, S. Jung, T. Jayaraman and M. Y. Choi 2023 *Bull. Korean Chem. Soc.* **44** 969.

[29] K.R.G. Lim, M. Shekhirev, B.C. Wyatt, B. Anasori, Y. Gogotsi and Z.W. Seh 2022 *Nat. Synth* **1** 601.

[30] M. Ghidiu, M.R. Lukatskaya, M.Q. Zhao, Y. Gogotsi and M.W. Barsoum 2014 *Nature* **516** 78.

[31] T. Li, L. Yao, Q. Liu, J. Gu, R. Luo, J. Li, X. Yan, W. Wang, P. Liu, B. Chen, W. Zhang, W. Abbas, R. Naz and D. Zhang 2018 *Angew. Chem. Int. Ed.* **57** 6115.

[32] O. Mashtalir, M.R. Lukatskaya, M.Q. Zhao, M.W. Barsoum and Y. Gogotsi 2015 *Adv. Mater.* **27** 3501.

[33] O. Mashtalir, M. Naguib, V.N. Mochalin, Y. Dall'agnese, M. Heon, M.W. Barsoum and Y. Gogotsi 2013 *Nat. Commun*. **4** 1716.

[34] M. Naguib, R.R. Unocic, B. L. Armstrong and J. Nanda 2015 *Dalton Trans.* **44** 9353.

[35] F. Han, S. Luo, L. Xie, J. Zhu, W. Wei, X. Chen, F. Liu, W. Chen, J. Zhao, L. Dong, K. Yu, X. Zeng, F. Rao, L. Wang and Y. Huang 2019 *ACS Appl. Mater. Interfaces* **11** 8443.

[36] J. Mei, G.A. Ayoko, C. Hu and Z. Sun 2020 *Chem. Eng. J.* **395** 125111.

[37] D. Wang, C.K. Zhou, A.S. Filatov, W.J. Cho, F. Lagunas, M.Z. Wang, S. Vaikuntanathan, C. Liu, R.F. Klie and D.V. Talapin 2023 *Science* **379** 1242.

[38] A. Sherryna, M. Tahir and Z.Y. Zakaria 2024 *Int. J. Hydrog. Energy* **51** 1511.

[39] K. Anja, Z. Alexander and G. Franziska 2022 *Front. Chem.* **9** 2296.

[40] J.H. Li, P. Hao, L. Bing, J.M. Cao, L.J. Ma and D.W. Jing 2023 *J. Colloid Interface Sci.*

641 309.

[41] X. Ruan, D. Meng, C. Huang, M. Xu, X. Wen, K. Ba, D.J. Singh, H. Zhang, L. Zhang, T. Xie, W. Zhang, W. Zheng, S.K. Ravi and X. Cui 2023 *Small Methods* **7** 2300627.

[42] B.S. Reghunath, S. Rajasekaran, S. Mathew, D. Pinheiro, K.R.S. Devi, S. Jung, T. Jayaraman and M.Y. Choi 2023 *Bull. Korean Chem. Soc.* **44** 969.

[43] B.T. Sun, P.Y. Qiu, Z.Q Liang, Y.J. Xue, X.L. Zhang, L.Yang, H.Z. Cui and J. Tian 2021 *Chem. Eng. J.* **406** 127177.

[44] G. Zuo, Y. Wang, W. L. Teo, A. Xie, Y. Guo, Y. Dai, W. Zhou, D. Jana, Q. Xian, W. Dong and Y. Zhao 2020 *Angew. Chem. Int. Ed.* **59** 11287.

[45] Y.J. Zhang, K.L. Zhou, C.Y. Yuan, H.J. Lv, H.F. Yin, Q. Fei, D.D. Xiao, Y.Z. Zhang and W.M. Lau 2024 *J. Colloid Interface Sci.* **653** 482.

[46] J.M. Li, L. Zhao, S.M. Wang, J. Li, G.H. Wang and J. Wang 2020 *Appl. Surf. Sci.* **515** 145922.

[47] Q.Z. Hou, M.Y. Wang, T.G. Li, Y.Q. Hou, K. Xuan and Y.M. Hao 2023 *Chem. Eng. J.* **464** 142566.

[48] J.X. Li, S. Wang, Y.L. Du and W.H. Liao 2018 *Ceram. Int.* **44** 7042.

[49] M. Ishfaq, A. Rasheed, S. Ajmal, G. Dastgeer, T. Naz, M.M. Baig and S.G. Lee 2024 *Ceram. Int.* **50** 9801.

[50] K. Roy, D. Ghosh, S. Maitra and P. Kumar 2023 *J. Mater. Chem. A* **11** 21135.

[51] Y.Z. Wu, J.W. Wu, C. Zhu, L. Zhang and J.H. Yan 2023 *Chem. Eng. J.* **465** 142798.

[52] J.B. Wu, J.W. Su, T. Wu, L. Huang, Q. Li, Y.X. Luo, H.R. Jin, J. Zhou, T.Y. Zhai, D.S. Wang, Y. Gogotsi and Y.D. Li 2023 *Adv. Mater.* **35** 2209954.

[53] W.Z. Wang and S. Gunasekaran 2024 *Chem. Eng. J.* **482** 148693.

[54] S. Kim, H. Shin, J. Lee, C. Park, Y. Ahn, H.J. Cho, S. Yuk, J.H. Kim, D.J. Lee and I.D.

Kim 2023 *ACS Nano* **17** 19387.

[55] A.Y.S. Tan, H.T.A. Awan, F.L. Cheng, M. Zhang, M.T.T. Tan, S. Manickam, M. Khalid and K. Muthoosamy 2024 *Chem. Eng. J.* **482** 148774.

[56] Z. Wang, G. Tan, B. Zhang, Q. Yang, S. Feng, Y. Liu, T. Liu, L. Guo, C. Zeng, W. Liu, A. Xia, H. Ren, L. Yin and S. Fan 2024 *Adv. Mater.* 2024 **36** 2307795.

[57] A. Usman, M. Qin, F. Xiong, W. Aftab, Z. Shen, A. Bashir, H. Han, S. Han and R. Zou 2024 *Small Methods* 2024 2301458.

[58] P. Das, Y.F. Dong, X.H. Wu, Y.Y. Zhu and Z.S. Wu 2023 *Sci. Bull.* **68** 1735.

[59] Y.P. Ren, X.L. Zhou, X.J. Gao, J.J. Si, W.H. Ren, C.X. Li, Q. Yang, Y.L. Zhou, F. Bai and W.W. He 2024 *Nano Today* **55** 102202.

[60] X. Zhao, Y. Chen, R. Niu, Y. Tang, Y. Chen, H. Su, Z. Yang, X. Jing, H. Guan, R. Gao and L. Meng 2024 Adv. Mater. 36 2307839.

[61] S. Zhang, L. Wu, W. Shi, J. Qin, W. Feng, Y. Chen and R. Zhang 2023 *Adv. Funct. Mater.* 2023 **33** 2302360.

[62] Q. Tang, T. Li, W. Tu, H. Wang, Y. Zhou and Z. Zou 2024 *Adv. Funct. Mater.* 2311609.

[63] S.H.W. Kok, J.L. Lee, L.L. Tan, W.J. Ong and S.P. Chai 2022 *ACS Materials Lett.* **4** 212.

[64] K.X. Gao, L.A. Hou, X.Q. An, D.D. Huang and Y. Yang 2023 *Appl. Catal. B* **323** 122150.

[65] A. Fujishima, and K. Honda, 1972 *Nature* **238** 37.

[66] H.P. Li, B. Sun, T.T. Gao, H. Li, Y.Q. Ren and G.W. Zhou 2022 *Chinese J. Catal.* **43** 461.

[67] H.S. Huang, Y. Song, N.J. Li, D.Y. Chen, Q.F. Xu, H. Li, J.H. He and J.M. Lu 2019 *Appl. Catal. B* **251** 154.

[68] Y.Z. Wu, J.W. Wu, C. Zhu, L. Zhang and J.H. Yan 2023 *Chem. Eng. J.* **465** 142798.

[69] Y.Y. Liu, H. Xiao and W.A. Goddard. 2016 *J Am Chem Soc.* **138** 15853.

[70] Z.R. Wang, Y. Zhang, Y.M. Chen, P. Wei, H.J. Wang, H. Yu, J.B. Jia, K. Zhang and C.

Peng 2023 *Appl. Surf. Sci.* **615** 156343.

[71] C. Peng, T. Zhou, P. Wei, H.Q. Ai, B.P. Zhou, H. Pan, W.K. Xu, J.B. Jia, K. Zhang, H.J. Wang and H. Yu 2022 *Chem. Eng. J.* **439** 135685.

[72] L. Wang, J. Ge, A. Wang, M. Deng, X. Wang, S. Bai, R. Li, J. Jiang, Q. Zhang, Y. Luo and Y. Xiong 2014 *Angew. Chem. Int. Ed.* **53** 5107.

[73] S.L, Xie, Z.L. Wang, F.L. Cheng, P. Zhang, W.J. Mai and Y.X. Tong 2017 *Nano Energy* **34** 313.

[74] H.R. Zhu, X.M. Fu and Z.Q. Zhou 2022 *ACS Omega* **7** 21684.

[75] S. Zong, J.C. Liu, J. Zheng, X.Y. Feng, L.L. Liu and Y.X. Fang 2023 *Int. J. Hydrog. Energy* **48** 34272.

[76] J. Prakash, P. Kumar, N. Saxena, Z. Pu, Z. Chen, A. Tyagi, G. Zhang and S. Sun 2023 *J. Mater. Chem. A* **11** 10015.

[77] Y.C. Wang, B.Y. Ren, J.Z. Ou, K. Xu, C.H. Yang, Y.X. Li and H.J. Zhang 2021 *Sci. Bull.* **66** 1228.

[78] T.Y. Huang, Z. Yang, S.Y. Yang, Z.H. Dai, Y.J. Liu, J.H. Liao, G.Y. Zhong, Z.J. Xie, Y.P. Fang and S.S. Zhang 2024 *J Mater Sci Technol* **171** 1.

[79] H. Zhang, Y. Gao, S. Meng, Z. Wang, P. Wang, Z. Wang, C. Qiu, S. Chen, B. Weng and Y. M. Zheng 2024 *Adv. Sci.* 2400099.

[80] M. Zhang, Y.X. Zhang, L. Ye, Z.H. Yu, R.Y. Liu, Y.N. Qiao, L.H. Sun, J.F. Cui and X.B. Lu 2023 *Appl. Catal. B* **330** 122635.

[81] G.Q. Zhang, Z.Q. Wang, T. He, J.L. Wu, J.Z. Zhang and J.H. Wu 2022 **442** 136309.

[82] C. Liu, W. Xiao, G.Y. Yu, Q. Wang, J.W. Hu, C.H. Xu, X.Y. Du, J.G. Xu, Q.F. Zhang and

Z.G. Zou 2023 *J. Colloid Interface Sci.* **640** 851.

[83] L. Wu, Q. Wang, T.T Zhuang, Y. Li, G.Z. Zhang, G.Q. Liu, Fe.J. Fan, L. Shi and S.H. Yu 2020 *Nat Commun* **11** 5194.

[84] Y.M. Sun, Y. Hao, X.Y. Lin, Z.H. Liu, H.Y. Sun, S.H. Jia, Y.H. Chen, Y.S. Yan and X.F. Li 2024 *J Colloid Interf Sci* **653** 396.

[85] Q. Li, H.H. Zhang, H.J. Gu, Y.Y. Cui, R.H. Gao and W.-L. Dai 2024 *Acta Phys. -Chim. Sin.* 2402016.

[86] H.J. Gu, H.H. Zhang, X.L. Wang, Q. Li, S.Y. Chang, Y.M. Huang, L.L. Gao, Y.Y. Cui, R.W. Liu and W.-L. Dai 2023 *Appl. Catal. B* **328** 122537.

[87] X.C. Wang, K. Maeda, A. Thomas, K. Takanabe, G. Xin, J.M. Carlsson, K. Domen and M. Antonietti 2009 *Nature Mater* **8** 76.

[88] H.T. Xu, R. Xiao, Ji.R. Huang, Y. Jiang, C.X. Zhao and X.F. Yang 2021 *Chinese J. Catal* **42** 107.

[89] K.L. Huang, C.H. Li, X.L. Zhang, L. Wang, W.T. Wang and X.C. Meng 2023 *Green Energy Environ* **8** 233.

[90] K. Zhang, D.Q. Li, H.Y. Cao, Q.H. Zhu, C. Trapalis, P.F. Zhu, X.H. Gao and C.Y. Wang 2021 *Chem. Eng. J* **424** 130340.

[91] L. Ding, Y.Y. Tang, S.Y. Wang, Y.Q. Zhang, X.Y. Chen and H.J. Zhou 2024 *J Colloid Interf Sci* **653** 1671.

[92] H. Yang, K. Dai, J.F. Zhang and G. Dawson 2022 *Chinese J. Catal* **43** 2111.

[93] Y.L. Li, Y.T. Sun, Y.X. Liu, T.F. Zheng, A.J. Li, G.G. Levchenko, W. Han, A.V.

Pashchenko, S.I. Sasaki, H. Tamiaki and X.F. Wang 2024 *J Colloid Interf Sci* **654** 1001.

[94] J. He, Y.J. Jo, X.L. Sun, W.G. Qiao, J. Ok, T.I. Kim and Z.A. Li 2021 *Adv. Funct. Mater.* **31** 2008201.

[95] Y.X. Liu, Y.L, Li, A.J. Li, Y. Gao, X.F. Wang, R. Fujii and S.I. Sasaki 2023 *J Colloid Interf Sci* **633** 218.

[96] C. Wu, W.X. Huang, H.M. Liu, K.L. Lv and Q. Li 2023 *Appl. Catal. B* **330** 122653.

[97] Y.M. Chen, Z.R. Wang, Y. Zhang, P. Wei, W.K. Xu, H.J. Wang, H. Yu, J.B. Jia, K. Zhang and C. Peng 2023 *ACS Appl. Mater. Interfaces* **15** 20027.

[98] J.X. Yang, W.B. Yu, C.F. Li, W.D. Dong, L. Jiang, N. Zhou, Z.H. Zhuang, J. Liu, Z.Y. Hu, H. Zhao, Y. Li, L.H. Chen, J.G. Hu and B.L. Su 2021 *Chem. Eng. J* **420** 129695.

[99] J.X. Bai, R.C. Shen, Z.M. Jiang, P. Zhang, Y.J. Li and X. Li 2022 *Chinese J. Catal* **43** 359.

[100] W.K. Xu, X.Y. Li, C. Peng, G.X. Yang, Y.H. Cao, H.J. Wang, F. Peng and H. Yu 2022 *Appl. Catal. B* **303** 120910.

[101] J.X. Bai, W.L. Chen, L. Hao, R.C. Shen, P. Zhang, N. Li and X. Li 2022 *Chem. Eng. J* **447** 137488.

[102] M. Tayyab, Y.J. Liu, Z.G. Liu, L.H. Pan, Z.H. Xu, W.H. Yue, L. Zhou, J.Y. Lei and J.L. Zhang 2022 *J Colloid Interface Sci* **628** 500.

[103] J.X. Bai, W.L. Chen, R.C. Shen, Z.M. Jiang, P. Zhang, W. Liu and X. Li 2022 *J Mater Sci Technol* **112** 85.